

THE H α -BASED STAR FORMATION RATE DENSITY OF THE UNIVERSE AT Z=0.84.

VÍCTOR VILLAR, JESÚS GALLEGO, PABLO G. PÉREZ-GONZÁLEZ, SERGIO PASCUAL
Universidad Complutense de Madrid, E-28040 Madrid, Spain

KAI NOESKE, DAVID C. KOO
Lick Observatory, University of California, Santa Cruz, CA 95064

AND

GUILLERMO BARRO, JAIME ZAMORANO
Universidad Complutense de Madrid, E-28040 Madrid, Spain
Draft version April 20, 2022

ABSTRACT

We present the results of an H α *near-infrared* narrow-band survey searching for star-forming galaxies at redshift $z = 0.84$. This work is an extension of our previous narrow-band studies in the optical at lower redshifts. After removal of stars and redshift interlopers (using spectroscopic and photometric redshifts), we build a complete sample of 165 H α emitters in the Extended Groth strip and GOODS-N fields with $L(\text{H}\alpha) > 10^{41}$ erg s⁻¹. We compute the H α luminosity function at $z = 0.84$ after corrections for [NII] flux contamination, extinction, systematic errors, and incompleteness. Our sources present an average dust extinction of $A(\text{H}\alpha) = 1.5$ mag. Adopting H α as a surrogate for the instantaneous star formation rate (SFR), we measure a extinction-corrected SFR density of $0.17_{-0.03}^{+0.03}$ M $_{\odot}$ yr⁻¹ Mpc⁻³. Combining this result to our prior measurements at $z=0.02$, 0.24 , and 0.40 , we derive an H α -based evolution of the SFR density proportional to $(1+z)^{\beta}$ with $\beta = 3.8 \pm 0.5$. This evolution is consistent with that derived by other authors using different SFR tracers.

Subject headings: galaxies: evolution – galaxies: high redshift – galaxies: starburst

1. INTRODUCTION

The cosmic Star Formation Rate (SFR) density evolution of the Universe is an important constraint on galaxy formation and evolution models. Deep redshift surveys have proved that star-formation activity substantially increases with redshift from $z=0$ to $z \simeq 1$ (see Ferguson et al. 2000, for a review). This behavior has been reproduced by current galaxy evolution theories (see the review by Baugh 2006).

Several tracers can be used to obtain SFRs at different redshifts: ultraviolet (UV) continuum, nebular lines such as [OII] λ 3727 or H α , total infrared (TIR), or radio continuum luminosities. For a summary of SFR density measurements, see Hopkins (2004) and Hopkins & Beacom (2006). In the redshift regime from $z \sim 1$ to $z = 0$, the observational data in the Far-IR and UV is now much more robust with the results from *Spitzer* (Pérez-González et al. 2005) and those from GALEX (Arnouts et al. 2005; Schiminovich et al. 2005) and the VVDS (Tresse et al. 2007).

Focusing on the H α SFR tracer, the local SFR density was first measured by Gallego et al. (1995, see also Pérez-González et al. 2003) using the UCM Survey (Zamorano et al. 1994, 1996). Similar values at $z=0$ have also been obtained more recently by the SDSS (Brinchmann et al. 2004) and SINGG (Hanish et al. 2006) projects. At $z=0.24$, Tresse & Maddox (1998) and Pascual et al. (2001) obtained similar SFR densities for a sample of CFRS galaxies and a sample se-

lected using a narrow band technique like ours. Recently, Shioya et al. (2007) also used the narrow band technique at this redshift, reaching fainter luminosities. Jones & Bland-Hawthorn (2001) used their narrow band counts obtained with a tunable filter to study the redshift range $z=0.0-0.4$. Glazebrook et al. (2004) also used a tunable filter to detect a total of eight emission-line galaxies in the Hubble Deep Field, three of them being H α emitters at $z = 0.40$. At $z \sim 1$, Glazebrook et al. (1999) obtained a pioneering result from near-IR spectroscopy of eight CFRS galaxies in the $0.79 < z < 1.1$ redshift range. Their results were completed by Tresse et al. (2002), who obtained near-IR spectroscopy with VLT for 30 galaxies with redshifts $0.5 < z < 1.1$. Doherty et al. (2006) have recently obtained an average H α luminosity for 38 galaxies at $0.77 < z < 1$ by stacking near-IR spectra where the H α emission was not individually detected (for most of the targets). Aperture and luminosity bias corrections are needed to compare SFR densities from such slit spectroscopy studies with other data. Slit-less spectroscopy from HST data for galaxies in the $0.7 < z < 1.9$ redshift range allowed the analysis of Yan et al. (1999) and Hopkins et al. (2000) for 33 and 37 emission-line galaxies, respectively. Ly et al. (2007) used several narrow band filters to study emission-line galaxies at different redshifts and through different emission-lines. Finally, Reddy et al. (2007) have estimated the SFRd at $z=2-3$ based on UV and FIR luminosity functions, also predicting the H α luminosity function from them.

Significant discrepancies have been found when comparing the values obtained from different studies and tracers, due to dust extinction, metallicity and differ-

Electronic address: viv,jgm,pgperez,spr@astrax.fis.ucm.es
Electronic address: koo,kai@uclolick.org
Electronic address: gbc,jaz@astrax.fis.ucm.es

ent spatial origins of the emission. The $H\alpha$ luminosity is an excellent tracer of the SFR (Kennicutt 1998; Charlot & Longhetti 2001). It is essential when computing the SFR of a galaxy from its optical spectrum (Moustakas et al. 2006). The $H\alpha$ luminosity shares with the UV and TIR emissions the dependence to the Initial Mass Function (IMF). $H\alpha$ -based SFRs are affected by obscuration but are not very sensitive to metallicity. The TIR is not affected by dust attenuation, but it may miss the unobscured star formation which may be an important fraction of the total in certain galaxies (Pérez-González et al. 2006). There are also large uncertainties linked to the estimation of the TIR emission (from 8 to 1000 μm) from monochromatic measurements (e.g., the 24 μm flux). In addition, other sources different from the recent star formation (old stellar populations, AGNs) contribute to the dust heating in unknown (difficult to quantify) amounts. The UV luminosity not only traces the current SFR but also relatively old stellar populations (Calzetti et al. 2005) and is heavily affected by obscuration. As shown by Bell (2003), obscuration corrected $H\alpha$ is consistent, within a factor of 2, with the summed SFRs estimated using the UV and TIR luminosities. Consequently, $H\alpha$ observations of galaxy samples with UV and TIR data provides an invaluable tool to understand the evolution of the SFR and the role of obscuration in the determination of global SFR for galaxies.

Our group measured the SFR density locally (Gallego et al. 1995) using a sample of $H\alpha$ -selected galaxies from the objective-prism UCM Survey (Zamorano et al. 1994, 1996). We then extended this measurement to $z \simeq 0.24$ (Pascual et al. 2001; Pascual 2005) and also $z \simeq 0.4$ (Pascual 2005), the maximum redshift for which $H\alpha$ can be reached with CCDs. To select the $H\alpha$ emitters, we successfully used our own optical narrow band filters tuned to the wavelength of the redshifted $H\alpha$ line. The goal of this paper is to extend our previous work to $z=0.84$ using a narrow band filter centered at 1.20 μm .

This paper is structured as follows. In Section 2, we present the data, the observations, and reduction process. In Section 3, we describe the different steps to select the final sample, including our simulations to analyze the sample biases. In Section 4, we describe the procedure to obtain the $H\alpha$ fluxes for each galaxy. In Section 5, we present the $H\alpha$ luminosity functions (corrected and uncorrected for extinction) and the star formation rate density. Finally, we summarize our results and conclusions in Section 6.

A concordance cosmology is assumed throughout this paper with $H_0 = 70 \text{ km s}^{-1} \text{ Mpc}^{-1}$, $\Omega_M = 0.3$, $\Omega_\Lambda = 0.7$ (Lahav & Liddle 2006). With this cosmology, 1'' at $z=0.84$ corresponds to 7.63 kpc, the typical surveyed volume for a 1% narrow-band filter is $\sim 130000 \text{ Mpc}^3 \square^{-1}$ and the Universe is 6.44 Gyr old.

2. DATA

2.1. Observations

This work is based on deep near-infrared imaging obtained with a broad- and a narrow-band filters. The narrow-band filter is the J-continuum (J_c) centered at 1.20 μm , corresponding to $H\alpha$ at $z=0.84$. The broad-

band filter is used to determine an approximate continuum level near the $H\alpha$ emission-line.

The survey was carried out with the near-infrared camera OMEGA-2000¹ on the 3.5m telescope at the Calar Alto Observatory (Almería, Spain) with the J and narrow-band filters. OMEGA-2000 is equipped with a 2k \times 2k Hawaii-2 detector with 18 μm pixels (0''45 on the sky, 15' \times 15' field of view). Three different 15' \times 15' pointings were obtained, two in the Extended Groth Strip (EGS) and another one in the GOODS-North field, in April 2005 and May 2006. The characteristics of these 3 pointings are shown in Table 1.

Each field was observed with a dithering pattern consisting of 20 different positions with typical relative offsets of 20''-30''. After that sequence, the telescope starts another observation block at the initial position (slightly offsetted to remove artifacts). With this combination of patterns, the telescope visits 400 different positions without repeating anyone. For the J -band, we co-added 15 images of 10 seconds each, for a total of 150 seconds at each position. For the narrow-band filter (J_c), 5 images of 30 seconds were coadded at each position, for a total of 150 seconds as well. The total average exposure time per pixel was ~ 7.2 ks in the J band and ~ 18 ks in the J_c filter.

2.2. Reduction

We used a combination of the IRAF package XDIMSUM and our own dedicated software for the reduction of the data. In a first iteration, the dithered images were dark subtracted and combined without shifting to produce a master flat-field. Pixels marked as cosmetic defects were not used in this computation. After the flat field correction, the sky was subtracted. In this first iteration, we used the median value of each image as the sky value. At this point, we checked the photometry and seeing for each individual image, discarding those images that presented the worst seeing or with low object signal due to the presence of clouds or low transparency. We then combined the remaining images to produce a final mosaic. In the combination, for each final pixel in the image, we rejected pixel values from the individual images that exceeded by 3σ the mean signal. This allowed us to get rid of cosmetic defects and cosmic rays. With this first final image, we produced an object mask by detecting all the sources with SExtractor (Bertin & Arnouts 1996). In a second iteration, we repeated the same process except that we changed the method to construct the flat-field and the sky images. This time, for the flat-field construction we combined the science frames rejecting, in addition to cosmetic defects, object pixels. The sky subtraction was performed with XDIMSUM, taking previous and subsequent images to compute the sky for each individual image. Object pixels and cosmetic defects were also excluded in the sky construction. In a third iteration, we normalized the science images dividing by the sky images before creating the flat-field. The new flat-field is then not affected by the shape of the sky. The rest of the process is the same as in the second iteration, obtaining the final science image.

The observing runs were not fully photometric and we had to use bright 2MASS stars to do the photometric cal-

¹ <http://www.mpia-hd.mpg.de/IRCAM/O2000/index.html>

TABLE 1
OBSERVED FIELDS

Field (1)	α (J2000) (2)	δ (J2000) (3)	area (4)	t_{exp} NB (5)	t_{exp} BB (6)	FWHM(") NB (7)	FWHM(") BB (8)	m_{lim} NB (9)	m_{lim} BB (10)
Groth2	14 17 31	+52 28 11	0.0468	17850	7200	1.1	0.9	20.54	22.30
Groth3	14 18 14	+52 42 15	0.0648	18000	7200	0.9	1.1	20.99	22.43
GOODS-N	12 36 40	+62 12 16	0.0622	20300	9000	1.0	0.9	20.83	21.89

NOTE. — (1) Field name (2) RA (J2000) (3) DEC (J2000) (4) Area (square degrees) (5) narrow-band exposure time (s) (6) broad-band exposure time (s) (7) narrow-band FWHM (") (8) broad-band FWHM (") (9) narrow-band limiting J_{VEGA} magnitude (3σ) (10) broad-band limiting J_{VEGA} magnitude (3σ)

ibration. We introduced a color-term because our J -filter was not exactly the same as the 2MASS J filter. However, the color term was very small in most cases, with ($J - J_{2MASS} < 0.08$). We estimated that zeropoint errors were lower than ~ 0.15 mag. The narrow-band filter was calibrated using the J -band as reference, assuming that the mean color for the bright objects was zero.

2.3. Additional data

In order to estimate photometric redshifts and extinctions, we have also used complementary datasets in both the GOODS-N and the EGS fields. For the GOODS-N, we have used optical and NIR data spanning from the U- to the HK_s -bands (UBVRIZ HK_s , Capak et al. 2004) and our own K_s imaging data (Barro et al., in preparation). *Spitzer* IRAC data and MIPS 24 μ m images were also used, jointly with GALEX observations in the far ultraviolet (150 nm; FUV) and near ultraviolet (230 nm; NUV) bands. In addition, we also used the *bv*z HST ACS imaging covering the whole field.

For the EGS, we used the multi-wavelength dataset published by the All-wavelength Extended Groth Strip International Survey (AEGIS, see Davis et al. 2007 for a detailed description). These data consist in CFHT *ugriz* imaging, CFHT *BRI* (Coil et al. 2004) observations, *vi* HST-ACS data, *Spitzer* IRAC and MIPS images, and GALEX FUV and NUV observations.

There is also a wealth of publicly available spectroscopic redshifts in both fields. For the EGS, the DEEP2 Galaxy Redshift Survey (Faber et al. 2003) obtained over 15,000 redshifts in the whole EGS. In the GOODS-N field, spectroscopy is available for $\sim 1,500$ sources (Wirth et al. 2004; Cowie et al. 2004; Reddy et al. 2006).

3. SAMPLE SELECTION

3.1. Color-magnitude diagram

Emission-line objects were selected by their excess flux when comparing the narrow band and the broad band images. The candidates were selected as those showing a clear flux excess. The criterion used was:

$$(m_{BB} - m_{NB}) > \mu(m_{BB} - m_{NB}) + n_\sigma \sigma(m_{BB} - m_{NB}) \quad (1)$$

where m_{BB} is the apparent magnitude in the broad-band filter, m_{NB} is the apparent magnitude in the narrow-band filter, μ is an offset parameter, i.e. the average deviation from the zero color, σ is the standard deviation of the color distribution, and n_σ is the level of significance. The offset parameter and standard deviation can be expressed as a function of the narrow-band magnitude, and

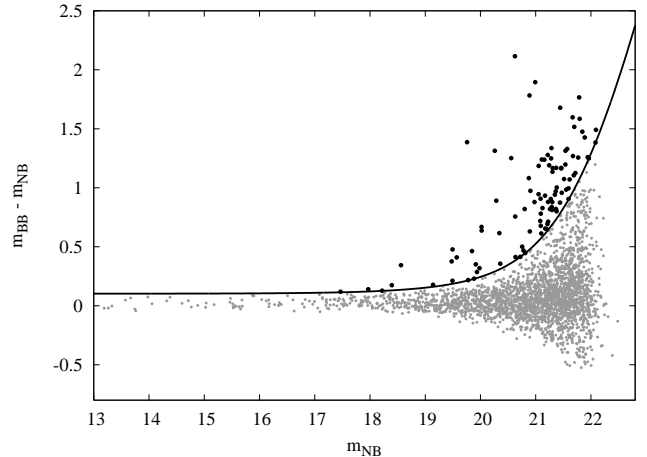


FIG. 1.— Color-magnitude diagram for the Groth3 field. Emission-line candidates are represented with black circles, and the rest of the objects are represented with grey circles. The 2.5σ selection curve is also plotted. Fluxes are measured within a four pixel diameter aperture.

they can be calculated directly from the distribution of objects. Thus, we have a certain curve, dependent on the narrow-band magnitude, above which objects are selected as emission-line candidates. In Figure 1, we show the color-magnitude diagram with the selection curve for one of our fields.

Fluxes in each band were measured within fixed circular apertures of different sizes. Thus, our measurements have the same spatial origin avoiding the mix of light from different regions in extended galaxies. The selection of the candidates was carried out using different apertures, typically ranging from the PSF FWHM to five times this quantity, for a total of 9-10 apertures.

The main goal in the selection process is to efficiently select emission-line objects avoiding (redshift and non-emission-line) interlopers. Taking advantage of the large spectroscopic surveys in both the EGS and GOODS-N fields, we studied the the level of significance and range of apertures that yielded better results.

In order to study the best level of significance, we created several selection curves with values of n_σ ranging from 1.5 to 3.0 in steps of 0.25. Each selection curve defines a sample of emitting candidates. We then obtained spectroscopic redshifts for each sample by cross-matching our selected samples with spectroscopic catalogs. The search radius was set to $1''$. The objects with spectroscopic redshift can be divided into those selected by an emission-line (i.e. selected by $H\alpha$, $[\text{OIII}]\lambda\lambda 5007, 4959$ or $[\text{OII}]\lambda 3727$ line flux), and those not selected by any of these emission-lines. The fraction of the former objects

over the total tell us how accurately we are selecting genuine emission-line galaxies. The final goal is to select the maximum number of objects without losing accuracy. Using the lowest significance level, we obtain a sample of candidates with the largest number of objects, but many of them could be redshift interlopers. Assuming that every object in the redshift range is an emission-line object, we can measure the fraction of objects recovered over the total in the lowest significance level. The best level of significance will be a compromise between accuracy and number of selected objects. In Figure 2, we show the results for each level of significance. We demonstrate here that a level of significance $n_\sigma=2.5$ is a good compromise between the number of selected emission-line objects and the accuracy of the selection.

To include as many different line emitters as possible, it is necessary to use several apertures. The smallest apertures are more adequate for the detection of small, low luminosity emission-line objects, since the corresponding fluxes are less affected by the sky noise. This is also the case for bright objects with high nuclear star formation. On the other hand, large, low surface brightness objects with extended star formation are better selected with the larger apertures. Large apertures measurements are very noisy for small objects, so apertures significantly larger than the object were not considered. Figure 2 shows the fraction of objects selected in each aperture over the total number obtained by taking into account all the apertures. In addition, we represent the accuracy at each aperture. If we select emission-line candidates in a $1.8''$ (4 pixels) diameter aperture, we recover $\sim 70\%$ of the objects in the final sample using all apertures. Thus, we are losing $\sim 30\%$ of the objects if we only use one aperture, even if it is the one that selects the highest number of objects. The accuracy in each aperture remains constant, even for the larger apertures where the sky noise could severely affect small objects fluxes. The reason is that we reject those objects selected in apertures much larger than its size.

3.2. Star-galaxy segregation

After selecting the candidates to be an emission-line at $z=0.84$, we must determine if the source is a star or a galaxy. The discrimination between stars and galaxies was carried out using eight different criteria. The main criterium was the STELLARITY parameter given by SExtractor in each optical and NIR band were the object was detected. Every object presenting an average value of the STELLARITY parameter higher than 0.95 was classified as a star.

In addition we used the following color criteria based on IRAC and NIR magnitudes (Eisenhardt et al. 2004; Rowan-Robinson et al. 2005): a) $[3.6] - [8.0] > -2$ and $[3.6] - [8.0] < -1$ and $[8.0] < 20.$, or $[3.6] - [4.5] > -1$ and $[3.6] - [4.5] < -0.5$ and $[4.5] < 19.5$; b) $[5.8] - [8.0] > -1$, $[5.8] - [4.5] < -0.2$ and $[8.0] < 20.$; c) $I - [8.0] < -1$ or $I - [3.6] < 1$ and $[3.6] < 18.$ or $I - [8.0] < -1$ and $[3.6] - [8.0] < -1$; d) $B - I > 2(I - [3.6]) + 0.070$; e) $J - K + 0.956 < 0.5$; and f) $[3.6]_{3''} - 0.460 - [3.6]_{auto} > -0.25$ and $[3.6] < 15.$ and $[3.6]_{3''} - 0.460 - [3.6]_{auto} < 0.2$, or $[3.6]_{3''} - [3.6]_{auto} < -0.25$, where $[\text{band}]_{3''}$ is the magnitude in a $3''$ diameter aperture, and $[\text{band}]_{auto}$ is the mag auto magnitude given by sextractor (an estima-

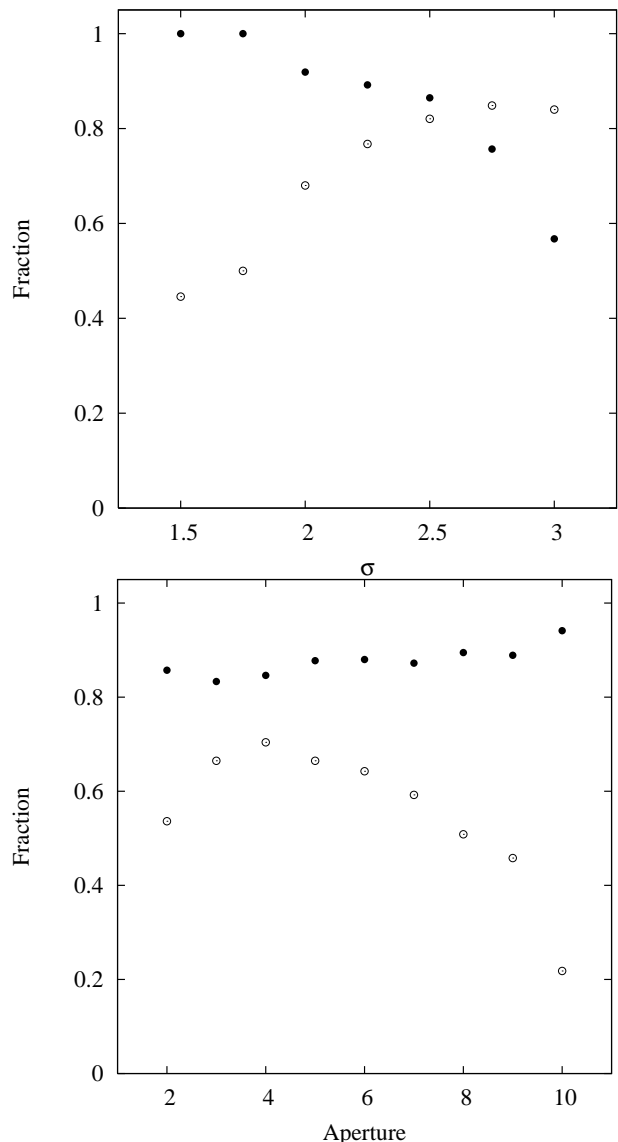


FIG. 2.— Left: Analysis of different significance levels n_σ . Open circles represent the fraction of emission-line objects in the total selected sample at each n_σ . Filled circles represent the fraction of emission-line objects selected at each n_σ level, considering the total as the number of objects selected at the lowest significance level, i.e. $n_\sigma=1.5$. Right: Selection results in different apertures. Open circles: fraction of total number of objects selected at each aperture over the total number obtained with all the apertures. Filled circles: fraction of confirmed emission-line objects.

tion of the integrated magnitude). The BzK criterion $(z - K)_{AB} < 0.3 \times (B - z)_{AB} - 0.5$ (Daddi et al. 2004) was also used.

Only 4 objects where classified as stars in the total sample of 243 candidates. Half of them were selected in the GOODS-N field and the other half in the field Groth2. This represents 1.6% of the whole sample, a clearly negligible fraction.

3.3. Photometric redshifts

Once the stellar objects have been removed from the sample, we tried to get rid of the objects outside the redshift range we are studying. We showed in Section 3.1 that we can have two types of redshift interlopers in our sample: a) those selected by other emission-lines; and b)

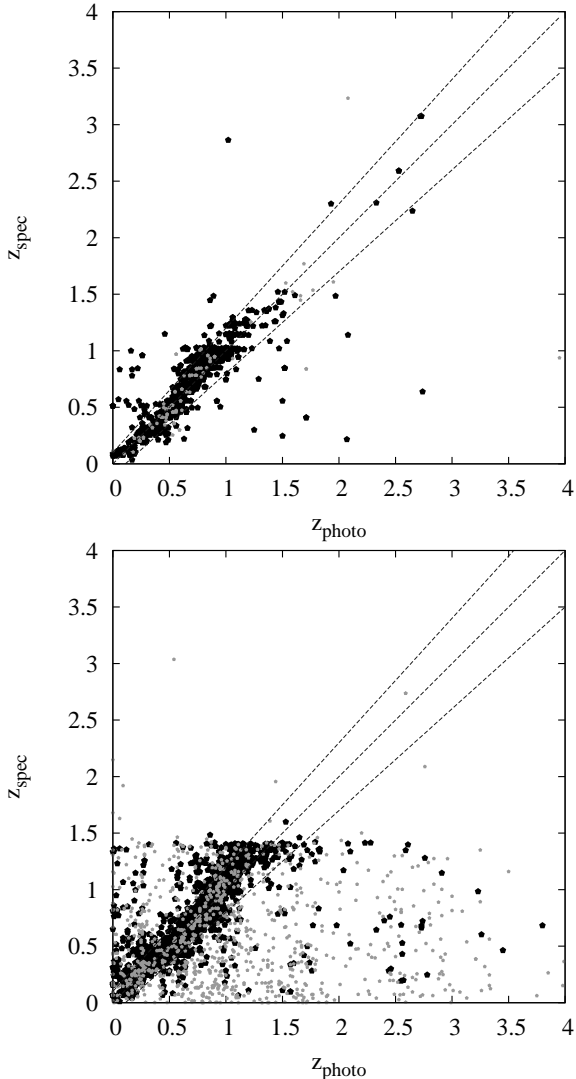


FIG. 3.— Comparison between spectroscopic and photometric redshift for sources selected in the J -band in the GOODS-N (left panel) and Groth fields (right panel). Black points are objects whose spectroscopic redshift quality is very good. Grey points have spectroscopic redshifts with low reliability flags. Note that, although it seems to be a lot of dispersion in the EGS field, 86% of the objects with reliable spectroscopic redshift fall within $\sigma_z/(1+z) < 0.1$ (dark lines in the figure), and 95% fall within $\sigma_z/(1+z) < 0.2$.

those selected due to noise or strange spectral features. Spectroscopic redshifts with enough quality were available for 98 out of 239 objects (241 if we include the stars). This means that there are 141 objects (59% of the entire sample) without spectroscopic data. Estimating photometric redshifts (despite their relatively high uncertainties compared to spectroscopic values) for these objects is important to get a highly complete and reliable sample of galaxies at $z \sim 0.84$.

We obtained photometric redshifts for our sources using the same method presented in Pérez-González et al. (2005) and appendix B of Perez-Gonzalez et al. (2007). First, we measured consistent (aperture matched) photometry in each band where the object was detected. Then, a set of templates (built with stellar population and dust emission models) was redshifted (in steps of $\Delta z = 0.1$) and convolved with the observed filters. A χ^2

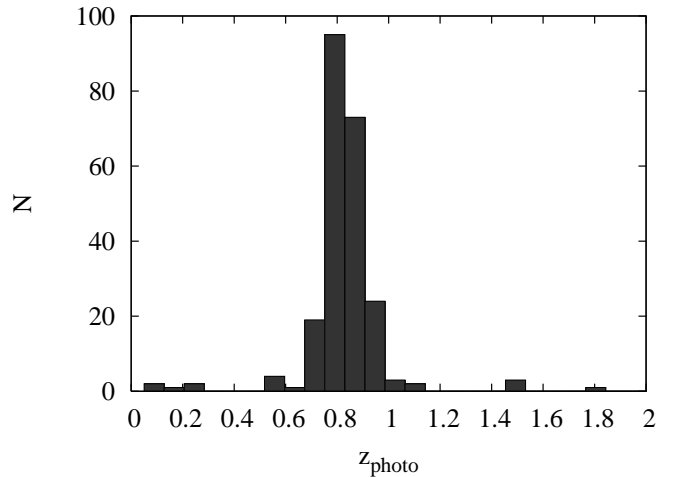


FIG. 4.— Photo-redshift histogram for all galaxies in our three fields with reliable spectroscopic redshift within our redshift range. Some of these objects have several peaks in the probability distribution that move them to the central Gaussian distribution.

minimization algorithm was used to estimate the most probable photometric redshift for each object. A preliminary step determining the $1.6\mu\text{m}$ bump feature helped to constrain the final solution. An additional constraint was imposed to the template that best fitted the data points: it had to be younger than the age of the universe at the given photometric redshift. The photometric redshift probability distribution was built with the best χ^2 values for each redshift. This probability distribution was very useful because some objects had two or even more peaks, making them compatible with different redshifts.

We estimated photometric redshifts for all the objects with spectroscopic redshifts detected in the J -band images. Figure 3 shows the comparison between spectroscopic and photometric redshifts for the GOODS-N and Groth fields. In the first panel, we show the comparison for the 1430 J -band sources with available spectroscopy in GOODS-N. Although there are some sources that lie quite far from the one-to-one relation, most of them have a photometric redshift in good agreement with the spectroscopic value. There is no evidence of a significant systematic error, given that the average difference $\delta z = z_{\text{spec}} - z_{\text{photo}}$ is 0.011, 90% of the objects with reliable spectroscopic redshift fall within $\sigma_z/(1+z) < 0.1$, and 97% fall within $\sigma_z/(1+z) < 0.2$.

The results for the EGS fields are shown in the second panel, with a total of 3810 sources. In this case, the quality of the photo-redshifts is very similar to that achieved in GOODS-N. The average difference between redshifts is $\delta z = -0.011$, 86% of the objects with reliable spectroscopic redshift fall within $\sigma_z/(1+z) < 0.1$, and 95% fall within $\sigma_z/(1+z) < 0.2$.

Due to the typical photometric redshift uncertainties, the objects with spectroscopic redshift in the redshift range of interest (the one corresponding to the $\text{H}\alpha$ emission for our NB filter) are spread over a much wider photo-redshift range. Figure 4 shows the histogram of photometric redshifts for the galaxies with spectroscopic redshifts within our filter's range. Most of the sources are close to the expected spectroscopic value of $z=0.84$ with some outliers. However, some of these outliers presents peaks in the probability distribution that shift them close

to the spectroscopic redshift. The mean (median) photo-redshift value of the distribution plotted in Figure 4 is $z_{\text{photo}}=0.822$ (0.820), whereas $z_{\text{spec}}=0.839$ (0.838). The difference is $\delta z=0.017$ (0.018), and the standard deviation for the photometric redshifts is 0.16.

Objects with a measured spectroscopic redshift outside the range covered by the filter were removed from the sample. Sources with no spectroscopic redshift and photometric redshift $z_{\text{photo}}<0.5$ or $z_{\text{photo}}>1.1$ were also discarded. Note that we checked the photo-z probability distribution for each of these sources and, in the cases where there was a peak at $0.5<z_{\text{photo}}<1.1$, it was introduced again in the sample. Finally, eight galaxies without spectroscopic nor photometric redshift were kept in the final sample.

After the removal of stars and redshift interlopers, the final sample of H α emitters at $z\sim 0.84$ has 165 objects: 51 in Groth3, 56 in Groth2 and 58 in GOODS-N. Of these, 165 galaxies, 79 (58%) are confirmed spectroscopically. Table 3 lists the objects in the final sample. The [OII] $\lambda 3727$ and [OIII] $\lambda\lambda 4959,5007$ emitters will be analyzed elsewhere.

3.4. Survey detection limits and completeness

The narrow-band technique to select emission-line galaxies at different redshifts has been extensively used over the last years. However, most of the times, the line flux detection limit is not consistently determined. The problem is that two different images are used and that each line flux could come from different combinations of narrow and broad band fluxes (i.e., galaxies could cover a wide range in equivalent widths).

In this work, we decided to tackle this problem performing simulations of the selection and measurement processes, in order to determine: a) the completeness of our selection; b) corrections for incompleteness in the luminosity function; and c) systematic errors that could lead to erroneous line flux measurements.

The method consisted in introducing a well known sample of fake galaxies in the science images and, working exactly in the same way as we do with the real images, check whether or not we recover the original properties of the fake sample.

The analysis of the HST morphology of our sample (Villar et al, in preparation) shows that most of our galaxies are disk, and that a significant fraction of the global star formation (typically less than 50%, with a mean value of 30%) is distributed in several star forming regions (being the mean number 5) covering the whole galaxy. We used this information to model disks with star formation distributed in five star forming regions, randomly distributed, within the galaxy's half light radius. This produces models of galaxies with highly concentrated as well as more extended and diffuse star formation. We used an exponential law for the disks, limiting the models to three different half light radius and three different inclinations. The star forming regions were modeled with Gaussian profiles and a half light radius of 600pc, which is the average radius we found in the morphological study. In Table 2, we give the range of parameters covered by the models. The fake galaxy images were constructed using GALFIT (Peng et al. 2002), convolving the model with the field's PSF. No additional noise was added to the models because the main source

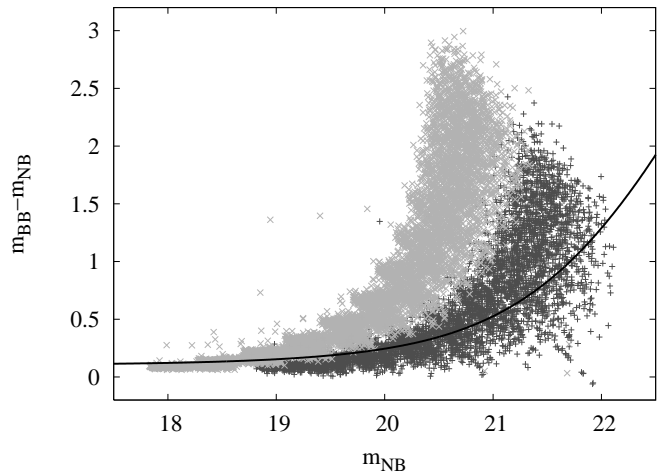


FIG. 5.— Color-magnitude selection diagram of simulated objects in the Groth3 field. The dark-grey points have $f_l=10^{-16}$ erg s $^{-1}$ cm $^{-2}$ and the light-grey ones have $f_l=1.5\times 10^{-16}$ erg s $^{-1}$ cm $^{-2}$. All magnitudes were measured in circular apertures for 4 pixels diameter. The solid line is the selection curve for this field and aperture size, with only objects above it considered as candidates (for this aperture).

TABLE 2
SIMULATIONS: RANGE OF PARAMETERS

Physical property	Range
Log Line flux(erg s $^{-1}$ cm $^{-2}$)	-15.1 – -16.5
H α equivalent width (Å)	10 – 2500
Effective radius (kpc)	2.5, 5.0, 7.5
Inclination ($^{\circ}$)	0, 45, 70

of noise for faint objects in our images was the sky background level. For each combination of parameters, we inserted 200 fake galaxies in the science image. We then carried out the detection of candidates in the standard way.

For a certain line flux, we have different narrow-band and broad-band fluxes. The magnitudes for each band are given by:

$$m_{NB} = C - 2.5 \log(f_c + f_l/\Delta_{NB}) \quad (2)$$

$$m_{BB} = C - 2.5 \log(f_c + f_l/\Delta_{BB}) \quad (3)$$

where C is the zero-point, f_c is the continuum flux per wavelength unit, f_l is the line flux and Δ_{NB} and Δ_{BB} are the narrow- and broad-band filter effective widths. Objects with the same line flux present different narrow-band magnitudes with a maximum value given by $m_{NB} = C - 2.5 \log(f_l/\Delta_{NB})$. In Figure 5, the different locations in the color-magnitude diagram are shown for objects with the same flux level simulated in the Groth3 field. The fluxes were measured in apertures of 4 pixels in diameter and the corresponding selection curve is also shown. We can see that the color, i.e., the equivalent width, increases with narrow-band magnitude. The reader should note that low equivalent width objects are not selected by our method. However, these sources also present bright J -magnitudes and they are not relatively very numerous, so the completeness will not be seriously affected. The fluxes for the faintest sources are recovered with less accuracy and the dispersion becomes larger,

preventing the selection of the whole fraction of objects.

In addition, Figure 5 shows that there is an upper limit to the color that decreases with narrow-band magnitude. The explanation is that high equivalent widths imply very faint fluxes in the broad-band image. Consequently, these objects would not be selected by our technique, since we need a simultaneous two band detection to assure the existence of the source. It is possible, however, to use the narrow-band image to detect all objects and then measure at the same position in the broad-band image. We did not apply this method because the alignment of the images was not good enough throughout the whole image, producing wrong centered apertures in the broad-band images in some regions, which lead to incorrect results. A refinement of the alignment process could not be done without substantial transformation of the images, which could alter the final results. We conclude that we may have missed faint galaxies with large equivalent width values undetected in the J -band. In order to analyze this systematic detection effect, we checked the images looking for objects only detected in the narrow-band images. We could not find any reliable candidate. Moreover, the maximum observed equivalent width measured in our sample is 1077\AA , with the rest of the sample below 600\AA . This is in good agreement with the results found in Gallego et al. (1995), Tresse et al. (2002), and Pascual (2005). A deep narrow band survey looking for Ly α emitters at redshift $z=8.8$ (Willis & Courbin 2005) did not find any population of high EW($H\alpha$) emitters. However, this survey was carried out over a small area. Our survey covers a much wider area and confirm these previous results.

Figure 6 (left) shows the fraction of selected objects for the different surveyed fields. Each panel correspond to a different field and shows the completeness for different half light radius. The completeness curve shows a smoother decline than that we can find in magnitude completeness studies. The reason is that in the narrow-band technique, two different magnitudes are involved and for each line flux we span a wide range in broad- and narrow-band magnitudes (see Figure 5). Another important issue is the effect of increasing the half light radius. The completeness drops from $\sim 80\%$ to $\sim 50\%$ when we move from $r_{eff}=2.5$ kpc to $r_{eff}=7.5$ kpc in the GOODS-N field at $\log(l_f)\sim -15.65$, and would move to lower fractions for higher half light radii. However, this is not a major concern in our case, since 85% of galaxies present half light radius lower than 7.5 kpc, with all of them except one below 10 kpc (Villar et al., in preparation).

The simulations allowed us to check the reliability of the measured fluxes. For the objects that satisfy the selection criteria, there is a good agreement between the mean recovered value and the mean simulated flux (see Figure 6, right panel), even for the faintest line fluxes. The comparison between individual objects in each line flux bin give us a better estimation of the error than that determined with photometric errors. Error bars in figure 6 show the standard deviation in the recovered line flux, computed as the standard deviation of the absolute difference between recovered and simulated line fluxes. The errors clearly increase as we move to fainter line fluxes, ranging from a 10% relative error for the brightest

objects to a 60% for the faintest ones, although they keep below 30% up to $f(H\alpha+[NII])=5\times 10^{-17}$ erg s $^{-1}$ cm $^{-2}$.

4. $H\alpha$ LUMINOSITIES FOR $Z\sim 0.84$ OBJECTS

4.1. Line flux estimation

Emission-line fluxes were computed using:

$$f_l = \Delta_{NB} (f_{NB} - f_{BB}) \frac{1}{1 - \epsilon} \quad (4)$$

where f_{NB} and f_{BB} are total fluxes in the narrow- and broad-bands, f_l is the line flux (including $[NII]\lambda\lambda 6548, 6584$), Δ_{NB} is the width of the narrow-band filter computed following the procedure specified by Pascual et al. (2007), and ϵ is the ratio of the widths of the narrow- and broad-band filters.

To estimate the integrated emission-line flux of each galaxy, we used the whole set of apertures. The flux grows with aperture diameter until the end of the emission region or the sky are reached. Since galaxies present a variety angular sizes, apertures of different sizes must be used. For small objects, the maximum flux will be reached in a small aperture, whereas for large objects it will be reached in larger apertures. We visually checked the emission-line fluxes for each aperture in each galaxy to select the more reliable integrated emission-line flux.

$H\alpha$ luminosities were computed from the line fluxes. The underlying stellar absorption for $H\alpha$ has a negligible effect when compared with errors from photometry, so no correction was added (see Nakamura et al. 2004). Nitrogen contamination to the narrow-band flux was removed following the approach in Pascual et al. (2007). In that work, the shape of the narrow-band filter is considered when computing the average $[NII]$ contribution to the measured flux, assuming a certain $I([NII]\lambda 6584)/I(H\alpha)$ value. These authors assumed an average ratio $I([NII]\lambda 6584)/I(H\alpha)=0.32$, the mean value obtained for the UCM Survey sample (Gallego et al. 1997) and the galaxies in the Sloan Digital Sky Survey Release 4 (SDSS DR4 Adelman-McCarthy et al. 2006). In our case, we have used the SDSS DR4 to study the dependence of $I([NII]\lambda 6584)/I(H\alpha)$ with the equivalent width of $H\alpha$ plus the $[NII]$ contribution $[EW(H\alpha + [NII])]$. Figure 7 shows $\log(I([NII]\lambda 6584)/I(H\alpha))$ versus $\log(EW(H\alpha + [NII]\lambda 6584))$. There is a clear trend of decreasing $I([NII]\lambda 6584)/I(H\alpha)$ as we move to higher equivalent widths, which can be explained due to a metallicity decrease. The circles represents the mean values obtained from the SDSS sample. The dispersion remains at ~ 0.4 dex for equivalent widths below $\log(EW(H\alpha + [NII]\lambda 6584))=2$. For higher equivalent widths, the dispersion increases up to ~ 1 dex. This relation was used to estimate the $[NII]$ contribution to the emission-line flux measured in the narrow-band images for each of our sources, obtaining a mean (median) value of $I([NII]\lambda 6584)/I(H\alpha)=0.26$ (0.27), ranging from 0.04 to 0.4.

The $I([NII]\lambda 6584)/I(H\alpha)$ may evolve with redshift as galaxy populations could be very different in the past than local ones. However, changing this ratio by a factor of 2 implies $\sim 20\%$ - 30% variation in the $H\alpha$ line fluxes, which is of the order of the errors.

4.2. Reddening correction

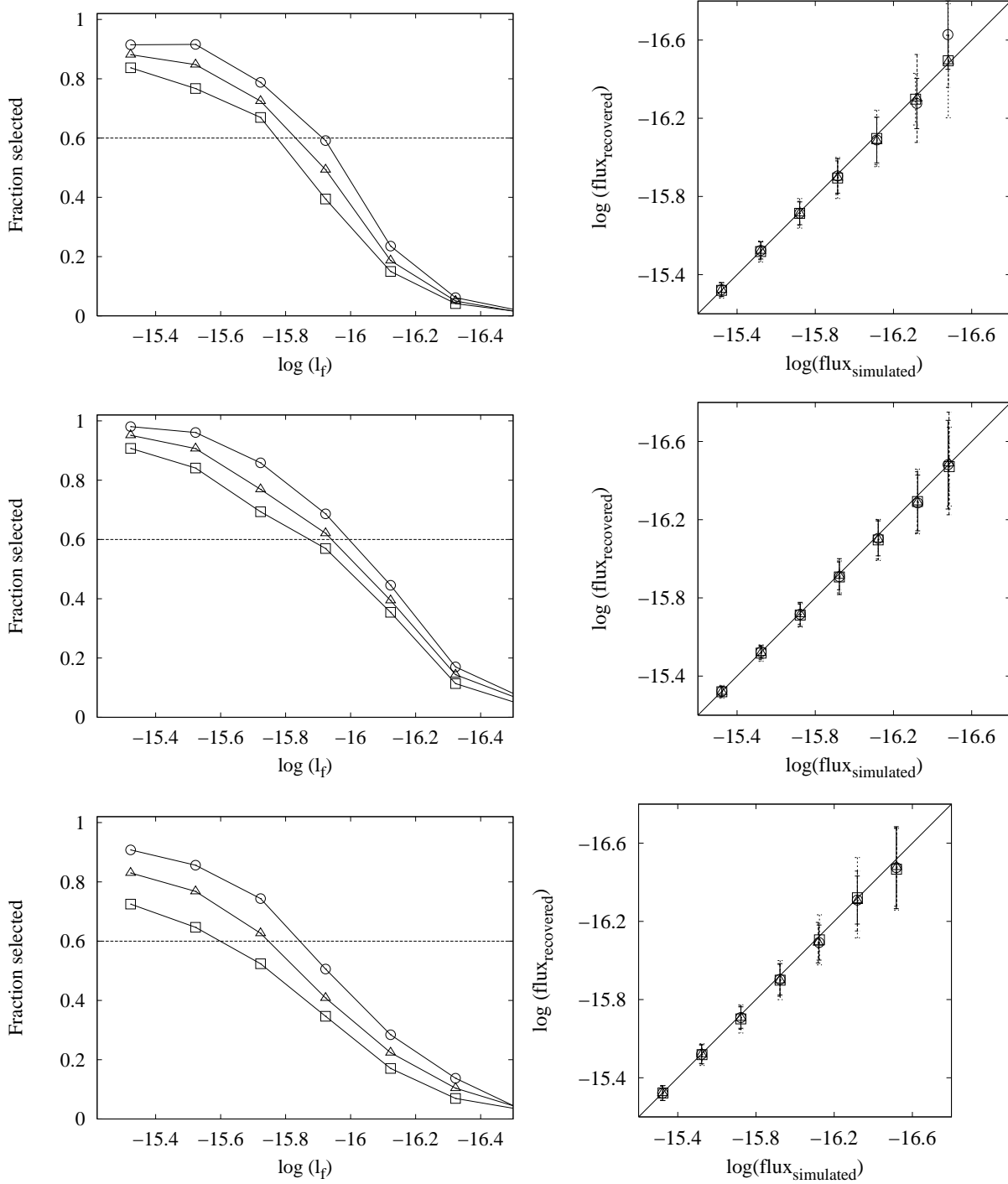


FIG. 6.— Completeness and line flux accuracy for each field surveyed. From top to bottom: Groth2, Groth3, GOODS-N. Left: Completeness versus line flux. Different symbols represent different half-light radius of the simulated sources: circles for 2.5 kpc, triangles for 5 kpc and squares for 7.5 kpc (assuming $z=0.84$). Right: Recovered flux versus input line flux. Symbols are the same as in the left panels.

Following Buat et al. (2005), we used the ratio ($F_{\text{dust}}/F_{\text{FUV}}$) to compute the extinction in the ultraviolet. Dust emission is given by $L(8-1000\mu\text{m})$ and can be estimated for the objects detected by MIPS, which traces the rest-frame continuum at $13\mu\text{m}$ in our redshift regime. To carry out this estimation, we first subtracted the stellar emission predicted by the stellar population templates (obtained in the photo- z determination) from the fluxes at rest-frame wavelengths redder than $\sim 4\mu\text{m}$

to obtain the pure emission of the dust. Then, we fitted this emission with Chary & Elbaz (2001) dust emission models. The model that best matched the observed dust emission colors [observed $F(24)/F(8)$] was selected, and we computed the TIR luminosity $L(8-1000\mu\text{m})$ from this model (for more details, see Perez-Gonzalez et al. 2007). The stellar population template, convolved with the FUV filter transmission curve, also give us the FUV rest-frame flux. With the $F_{\text{dust}}/F_{\text{FUV}}$ ratio, we com-

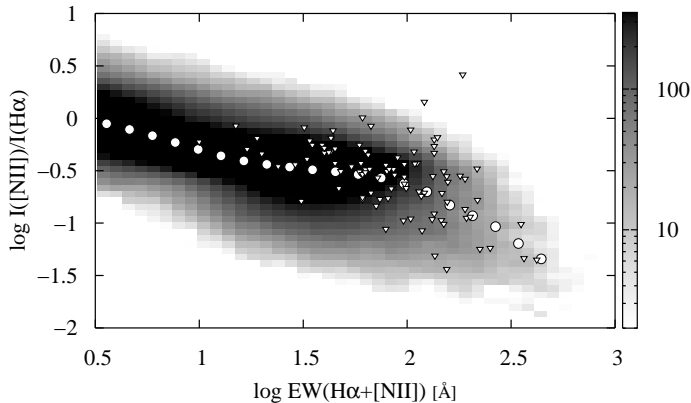


FIG. 7.— Ratio $I[NII]\lambda 6584/I(H\alpha)$ as a function of $EW(H\alpha + [NII])$ for the Sloan Digital Sky Survey (the number of galaxies is represented in gray scale) is represented in gray scale and the UCM survey (inverted triangles). The mean values for the SDSS are represented as circles.

pute $A(FUV)$ and then the extinction in $H\alpha$ applying the Calzetti extinction law (Calzetti et al. 2000), assuming that the attenuation of the stellar emission is 0.44 times the attenuation of the nebular emission. This law was empirically obtained from local starburst with star formation rates of up to a few tens $M_{\odot} \text{ yr}^{-1}$, very similar to our galaxies.

However, 86 objects were not detected at $24\mu\text{m}$, not allowing us to obtain the dust flux. In this case, we approached the problem from the ultraviolet side. The slope in the ultraviolet is another tracer of the dust obscuration and it is correlated with F_{dust}/F_{FUV} ratio, as Meurer et al. (1995) found for starburst galaxies. More recently, Gil de Paz et al. (2006) showed that the $(FUV - NUV)$ color, which relates to the UV slope (see Kong et al. 2004), is also correlated with the F_{dust}/F_{FUV} ratio. The $FUV - NUV$ color was computed convolving the best stellar population template with the appropriate filter transmission curves. Then, we estimated the F_{dust}/F_{FUV} ratio using the GALEX Ultraviolet Atlas of Nearby Galaxies. Each source in our sample was assigned the mean GALEX atlas F_{dust}/F_{FUV} at the same $(FUV - NUV)$. Figure 8 shows F_{dust}/F_{FUV} vs. $(FUV - NUV)$ for our 79 objects with MIPS detections. Late-type galaxies in the GALEX atlas have also been represented. Our sample follows, with higher dispersion, the general trend of nearby galaxies, although they are, in general, redder than the local sample, indicating that the extinctions are higher than those of the GALEX atlas sample. This also indicates that there is little evolution of this relation with redshift, not having a significant effect on our results. Moreover, considering the objects with extinctions available by both methods, we obtain similar mean extinctions: $A(H\alpha)=1.67$ mag and $A(H\alpha)=1.87$ mag using the UV slope and the infrared excess respectively.

The mean extinction in our sample is $A(H\alpha)=1.48$ mag, a value ~ 0.5 mag higher than the mean values obtained for the SDSS (Brinchmann et al. 2004) and UCM (Gallego et al. 1995) samples. This implies an increase in the typical extinction of star-forming galaxies with redshift of 0.5 mag from the local Universe to $z=0.84$.

Tresse et al. (2007) found that the dust obscuration at 1500\AA was $A(FUV)=2$ mag from $z=0.4$ to $z=2$, decreas-

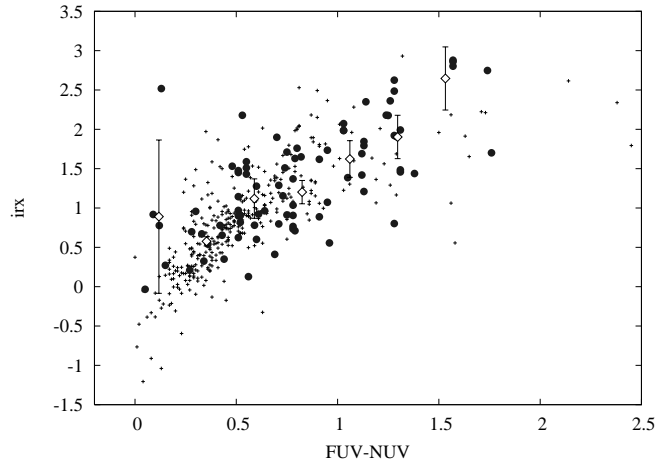


FIG. 8.— Dust flux to FUV flux ratio (irx) as a function of $FUV - NUV$ color, i.e. the UV slope. The crosses are the late-type galaxies in the GALEX Nearby Galaxy Atlas (Gil de Paz et al. 2006). Circles are objects in our sample that are detected at $24 \mu\text{m}$ by MIPS. Rhombus show the mean values and dispersion for our sample.

ing to $\sim 0.9-1$ mag for $z<0.4$. Our sample has a mean value of $A(FUV)=2.15$, in good agreement with these authors. They argue that the decrease in extinction at low redshift is due to the change of the dominant galaxy population. They show that the emission from early-type galaxies starts to dominate in the B -band below $z<0.5$, and they make the assumption that in the FUV the early-type population will still dominate. Therefore, as the dust content in early-type galaxies is much lower than in late-types, the amount of extinction will decrease as we move to lower redshifts.

However, the difference we find when comparing the mean extinction of our sample with that of local samples of star-forming galaxies cannot be explained with that argument. Brinchmann et al. (2004) showed that only 12% of the SFR density comes from galaxies with $D4000>1.8$, and only 2% from galaxies with $D4000>2$. Thus, only a very small fraction of the star formation can be located in old systems with very poor dust content. Moreover, Brinchmann et al. (2004) pointed out that these systems with high $D4000$ are probably spiral systems with significant bulges. In addition, Pérez-González et al. (2001) and Vitores et al. (1996) did not find any elliptical galaxy in the UCM sample and only 7% of lenticular objects. So, taking into account the previous discussion and the fact that our sample is dominated by disks, thus sharing the morphology of the SDSS and UCM samples, the higher extinction in our sample has to be caused by an increase in the dust content in the galaxies that host the star formation.

5. THE $H\alpha$ LUMINOSITY FUNCTION AT $Z=0.84$

5.1. The observed $H\alpha$ luminosity function

The $H\alpha$ luminosity function was calculated applying the V/V_{max} method (Schmidt 1968):

$$\phi(\log L_i) = \frac{1}{\Delta \log L} \sum_j \frac{1}{V(z)_j} \quad (5)$$

$$(6)$$

where L_i is the central luminosity in the bin i and $V(z)_j$

is the maximum volume in which object j can be detected.

To properly compute the volumes defined by the narrow-band filter, we followed the procedure described in section 5.3 of Pascual et al. (2007). These authors consider the volume in which an object would be detected in a narrow-band survey based on its position in the color-magnitude diagram, expanding the method to cope with several lines inside the narrow-band filter. The effect of the Nitrogen lines become important when the filter's transmittance falls and the $H\alpha$ line is detected there. In that case, one of the Nitrogen lines would be in the high transmittance region of the filter, increasing the total flux and, hence, the detection probability. To include this contribution, we considered the width of the filter affected by the Nitrogen lines as in Equation (34) of Pascual et al. (2007). If we consider and average volume determined only by the narrow-band filter's FWHM, we would be overestimating the surveyed volume by $\sim 20\%$ ($\sim 18\%$) on average (median), leading to a similar underestimation (i.e., a systematic error) of the LF points. It is also important to take into account the Nitrogen lines in the volume determination for each individual object. If not considered, volumes are subestimated by $\sim 40\%$ ($\sim 20\%$) on average (median).

The $H\alpha$ luminosity function with no extinction correction is shown in Figure 9. The best fit to a Schechter (1976) function yields the following parameters:

$$\begin{aligned}\phi^* &= 10^{-1.74 \pm 0.11} \text{Mpc}^{-3} \\ L^* &= 10^{41.69 \pm 0.07} \text{erg s}^{-1}\end{aligned}$$

We fixed $\alpha = -1.35$ (based on Tresse & Maddox 1998 and Shioya et al. 2007) as our LF did not reach faint enough luminosities to accurately determine it.

Errors were obtained from simulations. We computed a large number (~ 1000) of LFs, randomly changing the line flux for each object within a gaussian distribution, with σ determined by the object line flux error. The final errors in the LF are the standard deviations of the distributions obtained from the simulations. We apply this same method for the errors in the Schechter fit. We did simulations varying the LF within the errors distributions, obtaining distributions the Schechter parameters. The final errors in these parameters are the standard deviations of these distributions.

Figure 9 depicts the expected distribution of observed line fluxes for the $H\alpha$ line (since the Nitrogen correction was already applied). To correct for incompleteness, we computed the fraction of galaxies detected and selected at a certain line flux level (Section 3.4), what we call the completeness fraction. Then, we assumed that this fraction was the probability for a galaxy with these properties to be detected and selected in our sample. Thus, for each selected galaxy, we would expect the inverse of the completeness factor to be the real number density of galaxies. This is equivalent to multiplying each source's detection volume by its completeness factor. Thus, in the LF computation, we multiplied the detection volume of each galaxy by the completeness factor. The LF corrected for incompleteness is shown in Figure 9. The correction is more severe as we move towards fainter lu-

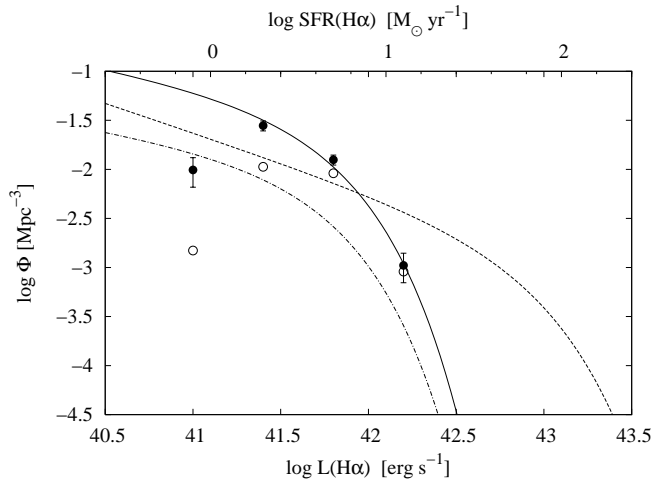


FIG. 9.— $H\alpha$ luminosity function not corrected for extinction (solid circles) with the best fit to a Schechter function (thick line). Open circles represent the derived LF before applying the completeness correction. For comparison Tresse et al. (2002) LF (dot-dashed line) and Hopkins et al. (2000) LF (dashed line) not corrected for extinction are also shown.

minosity bins. It is very strong in the faintest bin, but still it is most probably underestimated.

The LFs (not corrected for extinction) published by Tresse et al. (2002) and Hopkins et al. (2000) are also shown in Figure 9 (converted to the cosmology used in this work, see Hopkins 2004). Tresse et al. (2002) observed a sample of galaxies at $z \sim 0.7$ selected from the Canada-France redshift survey with $\text{EW}([\text{OII}]\lambda 3727) \geq 12 \text{\AA}$. Our LF is very similar to Tresse's, although ours extends to higher luminosities. Also, our LF presents a higher density at the faint end. This could be due to the fact that Tresse et al. (2002) applied a global completeness correction independent of the line flux. This was the best they could do, since they could not select the objects directly by their $H\alpha$ equivalent width or flux, but by $[\text{OII}]\lambda 3727$ equivalent width. A global completeness correction make the whole LF move to higher densities whereas a flux dependent completeness correction change the shape of the LF, raising the faint region. There is also another caveat in their selection: not all the $H\alpha$ emitters show $[\text{OII}]\lambda 3727 \text{\AA}$ emission. Yan et al. (2006) showed that in the SDSS survey, 20% of all emission-line galaxies with an $H\alpha$ detection have no $[\text{OII}]\lambda 3727 \text{\AA}$ emission. In this sense, if targets are selected in a spectroscopic survey using the oxygen line equivalent width, a considerable fraction of an $H\alpha$ selected sample would not be detected. On the other hand, $\sim 30\%$ of emission-line galaxies show oxygen emission with very low $H\alpha$ emission (22%) or no emission at all (8%).

Yan et al. (1999) and Hopkins et al. (2000) used the slitless spectroscopy technique to study emission-line galaxies at $z \sim 1$. Yan et al. (1999) selected 33 emitters at $0.75 \leq z \leq 1.9$. Their data was not deep enough to constrain α , so they assumed $\alpha = -1.35$. Hopkins et al. (2000) extended the study adding their deeper data to that of Yan et al. (1999). The LF was similar to that of Yan et al. (1999), although steeper. There is a huge discrepancy between our LF and theirs in the bright end of the LF, as they found many more brighter objects. Tresse et al. (2002) pointed out that, to some extent, it

could be an effect related to the Nitrogen correction. Indeed, the slitless spectroscopy did not allow a proper deblending of the $H\alpha$ line from the $[\text{NII}]\lambda 6548, 6584$ lines. However, we have the same problem and we estimate a lower density of high luminosity objects as well. Two explanations are possible: a change in the shape of the LF at higher redshifts or field to field variations. The redshift range surveyed in Yan et al. (1999) and Hopkins et al. (2000) is much larger than ours, reaching higher redshifts ($0.75 \leq z \leq 1.9$). Star-forming galaxies at $z \geq 1.4$ could be very different from those at $z=0.8$. For example, $\sim 30\%$ of the $H\alpha$ emitters at $z \sim 2$ studied by Erb et al. (2006) have $\log(L_{H\alpha}) > 42.5$, whereas our whole sample have lower luminosities. On the other hand, in the volume surveyed by these authors there could be a high density region due to cosmic variance. Probably, both effects are playing a role in the comparison.

5.2. The reddening corrected $H\alpha$ luminosity function

Two major effects are affecting our sample: extinction and field to field variance. The extinction correction was applied to each individual object and was explained in Section 4.2. Field to field variance implies galaxy density changes depending on the observed field. Within our three surveyed fields, we notice significant field to field variations. Figure 10 show the different LFs computed for each field. The Groth2 and GOODS-N fields show an overdensity over the Groth3 field. If we limit the comparison to the bins $\log(L_{H\alpha}) = \{41.5, 41.9\}$, which are less affected by low number statistics, the density of objects is ~ 2.3 and ~ 1.7 times higher in Groth2 and GOODS-N than in the Groth3 field, respectively. Takahashi et al. (2007) reported a similar variation among the COSMOS and Subaru Deep (SDF) fields for their $[\text{OII}]\lambda 3727$ emitters. In addition, we notice that none of our fields could be representative of the mean density of star forming galaxies in the Universe at this redshift.

In order to correct for the field to field variance effect we use photometric redshift and spectroscopic redshifts to estimate: a) the mean density of our fields with respect to other fields and b) the relative density of galaxies within our redshift range over this mean density.

We used photometric redshifts (Perez-Gonzalez et al. 2007, Pérez-González et al., in prep.) for the EGS, GOODS-N, Chandra Deep Field South (CDFs) and Lockman Hole (LH) to estimate the mean density in a redshift range centered at our redshift, ranging from $z=0.75$ to $z=0.9$. We used a redshift range wider than the narrow-band filter redshift range because photometric redshifts do not work properly in such a small range. We found that there was an overdensity of galaxies in both EGS and GOODS-N fields. The overdensity factor was ~ 1.05 and ~ 1.16 for GOODS-N and EGS respectively. This first estimation tell us that we are observing fields with a higher density of galaxies than the mean density in the redshift range $0.75 < z < 0.9$. However, at the small range covered by our narrow-band filter densities could be very different. Fortunately, spectroscopic redshift surveys are precise enough to reveal the structure in redshift ranges as small as our. Then, we measured the density ratio of objects with reliable spectroscopic redshift within our redshift range over those within $0.75 < z < 0.9$. For GOODS-N we found that this factor

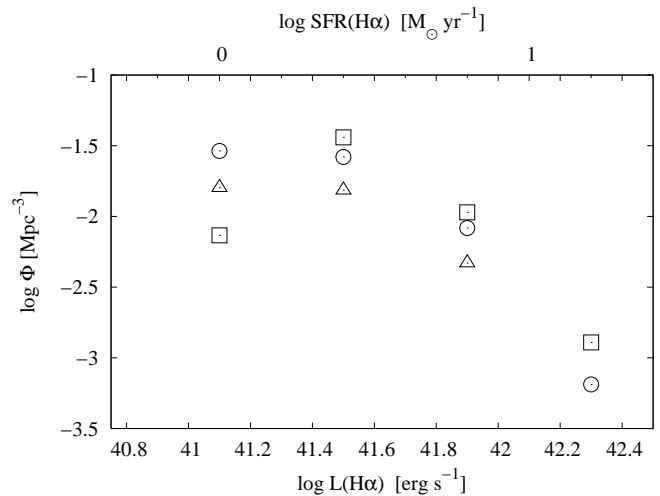


FIG. 10.— Derived LFs for the Groth2 (squares), Groth3 (triangles) and GOODS-N fields. The more populated points in the central region shows a density ratio of ~ 2.3 and ~ 1.7 for Groth2 and GOODS-N fields over Groth3 field.

was ~ 1.9 , which translates to ~ 2.0 when we take into account the density factor for GOODS-N over the mean density. For Groth2 and Groth3 fields we first measured the density factors between these fields and the whole EGS field for the redshift range $0.75 < z < 0.9$. We obtained ~ 1.07 and ~ 0.71 for Groth2 and Groth3 respectively, showing that could be high variations from field to field. Then, we measured the ratios between the galaxies within our redshift range and the galaxies in the wider redshift range, obtaining ~ 2.27 and ~ 1.30 , which become ~ 2.43 and ~ 0.93 for Groth2 and Groth3 fields respectively when compared to the whole EGS. Finally, applying the overdensity factor of the EGS, we obtained the final factors: ~ 2.8 and ~ 1.08 for Groth2 and Groth3 fields respectively.

We applied the same method to compute the luminosity function once we applied the extinction and field to field variance correction. The resulting best fit to a Schechter function gives:

$$\begin{aligned} \phi^* &= 10^{-2.76 \pm 0.32} \text{Mpc}^{-3} \\ L^* &= 10^{42.97 \pm 0.27} \text{erg s}^{-1} \\ \alpha &= -1.34 \pm 0.18 \end{aligned}$$

Note that this time we also fitted the faint-end slope. In the fitting process, we discarded the faintest and the brightest bins. The faintest bin was clearly affected by incompleteness. The brightest bin fell off the general shape of the best Schechter fit. Moreover, it contains only one object, which could be there due to a wrong estimation of the reddening or a photo- z outlier. Figure 11 shows the extinction-corrected LF derived in this work as well as Tresse et al. (2002) and Hopkins et al. (2000) corrected for extinction LFs. Tresse et al. (2002) applied an overall extinction correction $A_V=1$ mag obtained from the CFRS sample, except for two galaxies where high quality spectra were available and $f(H\beta)$ and $f(H\delta)$ could be measured. Hopkins et al. (2000) did not attempt the extinction correction though we can apply the typical correction $A(H\alpha)=1$ mag (see Pascual et al.

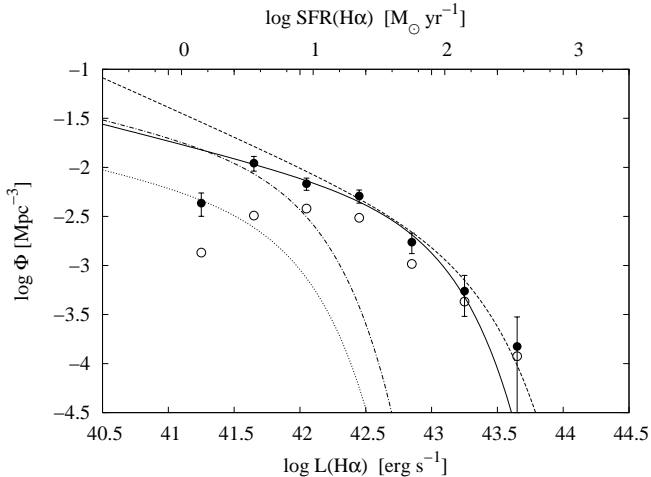


FIG. 11.— $H\alpha$ luminosity function corrected for extinction (solid circles) with the best fit to a Schechter function (thick line). Open circles represent the derived LF before applying the completeness correction. Gallego et al. (1995) local LF (dotted line) is also shown. Tresse et al. (2002) LF (dot-dashed line) and Hopkins et al. (2000) LF (dashed line) corrected for extinction are also shown. No correction was applied to the Hopkins et al. (2000) LF originally so we applied the typical $A(H\alpha)=1$ mag.

2007, and references therein) for this kind of surveys.

The change in the shape of the LF after correcting for extinction and field to field variance is evident. The typical $H\alpha$ luminosity has increased more than 1 dex, from $\log L^*(H\alpha)=41.69$ to $\log L^*(H\alpha)=42.97$, and the density ϕ^* has decreased from -1.74 to -2.76 , although this is explained in part because no density correction was applied to the observed LF. Now we can see a clear difference between Tresse et al. (2002) LF and this work in the bright regime.

In order to check if the bright regime may be affected by errors in extinction, we repeated the process to obtain the Schechter parameters, including a typical error in extinction of 0.3 mag. The effect on the Schechter parameters was found negligible.

Applying an individual extinction to each object modifies the whole shape of the LF, because the objects with highest corrected $H\alpha$ luminosities present high extinctions. Note that most of the previously published $H\alpha$ LFs assume an average extinction. However, for the total integrated SFRd, we obtain very similar results with both approaches (see section 5.3).

Now the shape of our LF is very similar to that of Hopkins et al. (2000), although they still present a higher density at faint luminosities. However, we have applied a global extinction correction to their LF, so we might expect a change in shape and an increase in luminosity if we make a careful extinction correction. Moreover, we obtain a mean extinction $A(H\alpha)=1.48$ in our sample and we expect even higher attenuation as we move to higher redshifts, so probably their LF would move to higher $H\alpha$ luminosities.

5.3. The $H\alpha$ -based cosmic star formation rate density

Once we have the LF, we can compute the $H\alpha$ luminosity density through:

$$\rho_L(H\alpha) = \phi^* L^* \Gamma(2 + \alpha) \quad (7)$$

where ϕ^* , L^* and α are the parameters obtained in the

Schechter fitting to the LF.

We convert this luminosity density to star formation rate density through the Kennicutt (1998) calibration.

We find that the inferred extinction-, field to field variance-corrected star formation rate density is $\dot{\rho}_* = 0.17^{+0.03}_{-0.03} M_\odot \text{ yr}^{-1} \text{ Mpc}^{-3}$.

As a consistency check, we checked that the observed and extinction corrected SFR densities differ by the mean extinction correction. We integrated the observed LF and applied the mean extinction correction. However, the observed LF was also affected by field to field variance so we applied a mean density correction (see section 5.2). The SFRd obtained in this case is $\dot{\rho}_* = 0.19^{+0.03}_{-0.03} M_\odot \text{ yr}^{-1} \text{ Mpc}^{-3}$, in good agreement with the previous value. This shows that although a mean extinction correction may not be the appropriate method to obtain real shape of the LF, it is enough to accurately determine the luminosity density or SFRd.

This value has not been corrected for AGN contribution as the effects are very small and other authors have not corrected their values either. The AGN contamination is a very difficult to solve problem, and a detailed analysis is out of the scope of this paper. We have tried to quantify how many of our galaxies harbor a luminous AGN by cross-correlating our sample with X-ray catalogs. We looked for X-ray detections in the Chandra 2Ms X-ray point source catalog (Alexander et al. 2003) in GOODS-N. We found 4 X-ray detections out of 58 candidates, within a $2''$ search radius. The amount of $H\alpha$ flux concentrated in these sources is 10% of the total flux in the whole GOODS-N sample, whereas their contribution to the number of galaxies is 8% (4/58). This result is in good agreement with Doherty et al. (2006) who found an AGN upper limit contribution of 9.5% to the flux density. Gallego et al. (1995) found higher values for the UCM local sample: 10% in number and 15% in flux density. In any case, it is important to notice that, although X-ray emission primarily come from the AGN, $H\alpha$ emission could come from a mixture of star forming processes and AGN activity. Hence, the fraction of $H\alpha$ flux concentrated in the X-ray detected sources is an upper limit to the $H\alpha$ flux coming from AGN activity. These X-ray catalogs could be missing very obscured AGN. We have checked the MIR SED of all our objects and none of them would qualify as a power-law galaxy (i.e., a heavily extinguished AGN; see, e.g., Alonso-Herrero et al. 2006). Still, even for the X-ray emitters, it would be impossible to quantify (with the data in our hands) whether the AGN or star formation dominate the $H\alpha$ (or MIR) emission.

We compare our result with other SFRd measured via $H\alpha$ line flux in figure 12. We took the different values from Hopkins (2004) except values at $z=0.24$ and $z=0.4$ that were taken from Pascual (2005) and the result at $z\sim 0.82$ by Doherty et al. (2006). The Pettini et al. (2001) value, obtained via $H\beta$, is also shown. In the Hopkins (2004) compilation, all SFRd values were corrected for extinction using a SFR dependent obscuration when the LF was available and the correction by the original authors (if any) was overall and SFR independent. If the LF was not available and no correction was made by the original authors, a mean obscuration correction of $A(H\alpha)=1$ mag was applied.

The closest values in redshift are those by Tresse et al.

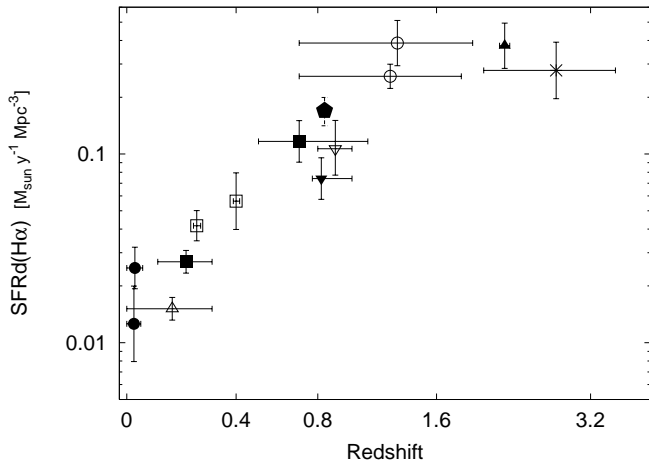


FIG. 12.— Evolution of the star formation rate density with redshift (scale is given by $\log(1+z)$) for estimations based on $H\alpha$ measurements. The dark pentagon is this work result. Other $H\alpha$ measurements come from Gallego et al. (1995) and Pérez-González et al. (2003) (filled circles), Sullivan et al. (2000) (triangle), Pascual (2005) (empty squares), Tresse & Maddox (1998) and Tresse et al. (2002) (filled squares), Doherty et al. (2006) (inverted filled triangle), Glazebrook et al. (1999) (inverted triangle), Yan et al. (1999) and Hopkins et al. (2000) (empty circles), Moorwood et al. (2000) (filled triangle), and Pettini et al. (2001) (star).

(2002), Doherty et al. (2006), and Glazebrook et al. (1999). Our result is systematically higher, about a factor of ~ 1.5 . However in the figure we can see that the difference between Tresse et al. (2002) and this work could be an evolution effect, as they follow the general trend in redshift (evolution will be discussed in more detail in Section 5.4). The other two points fall off the general trend. Doherty et al. (2006) value was corrected for incompleteness by a factor of ~ 3 due to the inherent difficulty of multi-object fiber spectroscopy observations. Only 9 out of 38 galaxies observed were clearly detected ($\geq 5\sigma$) and the others were stacked in order to get some information about $H\alpha$ low luminosity objects. They also had to apply aperture corrections, with a mean value of 2.4 but with some individual values above 4. In spite of all the efforts they put in to correct for incompleteness and flux loss, they could still be missing an important fraction of flux density. Another bias that could have affected their result is that the selection was made in the R band, which samples $\sim 3600\text{\AA}$ rest-frame (i.e. the U band), taking the precaution to select only targets with identified emission-lines. The U -band, although a good tracer of star forming galaxies (Moustakas et al. 2006), is not a direct tracer as can be the rest-frame UV. In addition, as pointed out in Section 5.1, 20% of objects with no $[\text{OII}]\lambda 3727$ emission have $H\alpha$ emission in the SDSS, so they could be missing a fraction of $H\alpha$ emitters. Glazebrook et al. (1999) SFRd is ~ 2 times lower than our value. However they only detected 8 galaxies with $H\alpha$ in emission, which could severely affect their results.

5.4. Star formation rate density evolution

It is obvious from figure 12 that a decrease in SFRd has occurred from $z \sim 1$ to the local Universe, being the latter ~ 10 times less active forming stars. It is common to parametrize the evolution of the SFR density with a power law: $\dot{\rho}_* \propto (1+z)^\beta$.

Combining just the $H\alpha$ -based SFR densities obtained

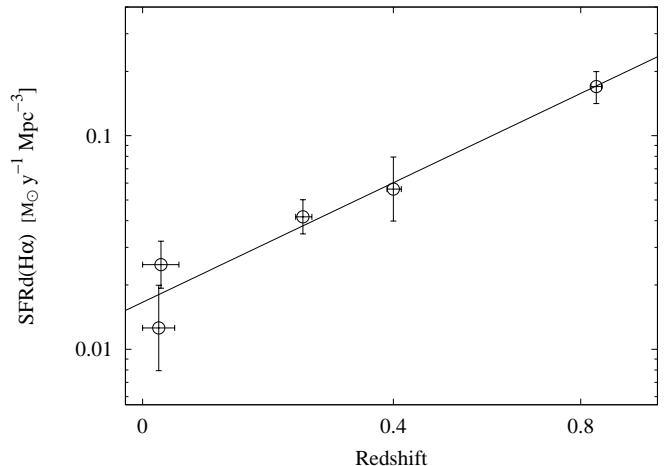


FIG. 13.— Evolution of SFRd measured by the UCM through the $H\alpha$ line (Gallego et al. 1995, Pérez-González et al. 2003, Pascual 2005 and this work). The line represents the best fit to a law $\propto (1+z)^\beta$ with $\beta=3.8$.

by our group at $z = 0.02$, $z = 0.24$, $z = 0.40$ and $z = 0.84$ for $H\alpha$ -selected samples, we obtain an evolution of the cosmic SFR density $\propto (1+z)^\beta$ where $\beta = 3.8 \pm 0.5$. The fitted power law is shown in figure 13. This β value is similar to the one estimated by Tresse et al. (2002) using $H\alpha$ observations, and by Pérez-González et al. (2005) for a thermal IR-selected sample. However, Tresse et al. (2002) value was calculated for an Einstein-de Sitter cosmology with $H_0=50 \text{ km}^{-1}$. The cosmology change softens this value to ≈ 3.5 (Doherty et al. 2006). Thus, we find a slightly higher value but still compatible within errors. Our value is also comparable to that of Hopkins (2004) who used data obtained with multiple star formation tracers and obtained $\beta=3.19 \pm 0.26$ for a luminosity dependent obscuration correction.

More interesting is to compare the evolution of the SFRd obtained through different estimators. In Figure 14 we plot the SFRd history obtained in $H\alpha$, IR (from Pérez-González et al. 2005) and UV (from Schiminovich et al. 2005). $H\alpha$ -based SFRd values are corrected for reddening while the UV values are not. Pérez-González et al. (2005) obtained $\beta=3.98 \pm 0.22$ for a IR selected sample and Schiminovich et al. (2005) obtained $\beta=2.5 \pm 0.7$, both up to $z=1$. Our $H\alpha$ measurement agrees quite well with that obtained with the IR sample. The UV slope is significantly lower, which could be caused by an evolution in the extinction properties with redshift, in the case the populations selected with each method were mainly the same.

There is another interesting question that arises when comparing populations selected with different observables: are we selecting the same objects or are there substantial differences?

To answer this question, we have considered the galaxies detected by MIPS and having a reliable spectroscopic redshift. There are 11, 2 and 18 objects in Groth2, Groth3 and GOODS-N respectively that are within our filter redshift range, are detected by MIPS, but not selected in our survey. This implies a 17%, 8% and 47% of the total $24\mu\text{m}$ flux in spectroscopically confirmed MIPS galaxies (at $z \sim 0.84$), corresponding the lowest fraction to our deepest field and the high fraction to our shallowest field. Thus, the extinction in these objects could

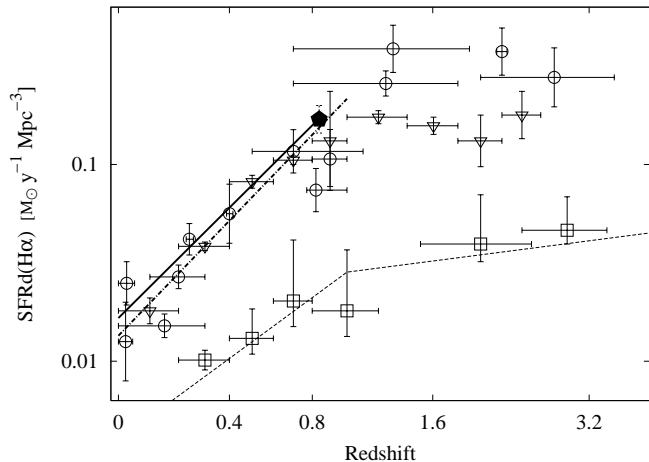


FIG. 14.— Evolution of the star formation rate density with redshift for estimations based on $H\alpha$, IR and FUV measurements. The dark pentagon is this work result. Other $H\alpha$ measurements (open circles) come from Gallego et al. (1995), Pérez-González et al. (2003), Sullivan et al. (2000), Pascual (2005), Tresse & Maddox (1998), Tresse et al. (2002), Doherty et al. (2006), Glazebrook et al. (1999), Yan et al. (1999), Hopkins et al. (2000), Moorwood et al. (2000) and Pettini et al. (2001). IR measurements (Pérez-González et al. 2005) are represented as open triangles and FUV estimations (Schiminovich et al. 2005) as open squares. The derived evolution law is represented as a thick line for $H\alpha$, a dashed line for UV and a dot-dashed line for IR.

make their $H\alpha$ flux fall below our detection limits, being worst for the shallower fields. However, the fraction in GOODS-N is still quite high to be explained by the different field depths. The explanation comes from the different extinction for the objects in these fields. Whereas for the Groth fields we have a mean $\overline{A}(H\alpha)=1.75$ mag, somewhat higher than the mean value for the whole sample, for the GOODS-N field this value is $\overline{A}(H\alpha)=3$ mag.

On the other hand, we are missing 11, 2 and 22 objects detected in the GALEX NUV-band which is very close to rest-frame FUV (a good estimator of the SFR). Most of these objects are missed because they fall below our detection limit. GALEX reach smaller SFRs, but only in the case of low attenuation. However, some objects show UV emission corresponding to a star formation rate that could be selected by our method. These missed objects could also be post starburst (that over predict current star formation) although there is no $H\alpha$ emission.

The opposite case is also present. We detect 23 (41%), 32 (63%) and 20 (34%) objects (including those with only photometric redshift) that do not show MIPS $24\mu\text{m}$ emission. The mean star formation rate for these objects is 2.8, 2.2 and $2.6 M_{\odot} \text{ yr}^{-1}$ with mean extinctions of $H\alpha$ of 1.0, 0.9 and 1.3 mag, thus having a mean corrected star formation rate of 7.0, 5.0 and $8.6 M_{\odot} \text{ yr}^{-1}$. These values are below the 80% completeness limit of the MIPS instrument in these fields: $83 \mu\text{Jy}$ which corresponds to $\sim 10 M_{\odot} \text{ yr}^{-1}$ (Pérez-González et al. 2005). When considering the UV emission there are 37(66%), 28(55%) and 26(44%) objects not detected in the GALEX NUV band. The mean $H\alpha$ star formation rate for these objects is 2.7, 2.5 and $3.45 M_{\odot} \text{ yr}^{-1}$ with the following mean extinctions: 1.5, 1.5 and 1.6 magnitudes in $H\alpha$. If we translate these SFRs to observed SFRs in the UV we obtain 1.4, 1.34 and $1.7 M_{\odot} \text{ yr}^{-1}$. These low SFRs are similar to the detection limit for the GALEX NUV-band

($\sim 1.5 M_{\odot} \text{ yr}^{-1}$) at $z=0.84$ based on the analysis of the GALEX catalog.

As we have shown, the most significant loss is the FIR emitters because they have high SFRs, but lie below our detection limit due to the presence of dust. We notice that although we are losing a fraction of the FIR objects our completeness correction is also recovering a fraction of them. The UV objects not recovered in our sample are very faint and contribute to the low luminosity regime of the luminosity function. On the other hand, FIR and UV surveys miss a significant fraction of objects. In the case of FIR it is worth to notice that, although we are missing a fraction of star forming galaxies, we obtain a very similar SFRd value to that of Pérez-González et al. (2005) (even higher). Hence, the objects not detected by MIPS with lower SFRs are playing a more important role than that estimated by Pérez-González et al. (2005). We conclude that our work is complementary to FIR and UV surveys, as it goes fainter than FIR detection limits and is not as affected by extinction as the UV.

6. SUMMARY AND CONCLUSIONS

Using an $H\alpha$ selected sample of star-forming galaxies we have estimated the $H\alpha$ luminosity function for the Universe at $z = 0.84$. This work is the continuation of previous surveys where our group used the $H\alpha$ emission to select representative samples of star-forming galaxies at intermediate redshifts. We argue that, since the $H\alpha$ emission provides a good estimate of the instantaneous star formation, the galaxies have been selected in a homogeneous way up to $z \sim 1$ by their current SFR. Therefore, we can use the $H\alpha$ luminosity function to determine the “current SFR function” describing the number of star-forming galaxies as a function of their SFR. Integrating over all $H\alpha$ luminosities (or SFRs) we determine the current SFR density for galaxies.

A total of 165 objects have been selected as $H\alpha$ emitters using the narrow band technique. We have tested the reliability of our emission-line candidates in three different ways: 1) analyzing the use of photometric apertures of different sizes; 2) carrying out a star-galaxy segregation; and 3) estimating photometric redshifts.

Line luminosities have been corrected for Nitrogen contribution and dust reddening. To correct for Nitrogen flux contamination, we used the SDSS sample to estimate the mean $[\text{NII}]$ to $H\alpha$ flux ratio for a given $\text{EW}(H\alpha + [\text{NII}])$. For the dust reddening correction, we proceeded in several steps: for the objects with MIPS detection, we estimated the total infrared luminosity and a synthetic FUV flux from templates and then compute the IRX ratio, which is related to the extinction in the FUV band. If the object was not detected in MIPS we used the UV slope, given by FUV-NUV (Gil de Paz et al. 2006). We found a mean extinction for the whole sample $A(H\alpha)=1.45$ mag, ranging from 0 to 4.16.

We performed simulations to determine the limiting flux and completeness corrections. The limiting fluxes vary from field to field from $8 \times 10^{-17} \text{ erg s}^{-1} \text{ cm}^{-2}$ to $14 \times 10^{-17} \text{ erg s}^{-1} \text{ cm}^{-2}$ for a 70% completeness level. The completeness correction was applied to the computation of the extinction not corrected and corrected LF.

We computed the observed LF not corrected for extinction, obtaining the following parameters when fitting to a Schechter function: $\phi^* = 10^{-1.74 \pm 0.11} \text{ Mpc}^{-3}$,

$L^* = 10^{41.69 \pm 0.07}$ erg s⁻¹. We fixed the low-luminosity slope $\alpha = -1.35$ because our LF was not deep enough. Our LF has higher density than that of Tresse et al. (2002), that could be explained by an evolutionary effect due to the different mean redshifts explored or by the selection method in each case: directly by H α in this work whereas they had to use the *I*-band and spectroscopic redshifts. Yan et al. (1999) and Hopkins et al. (2000) LFs extend to higher luminosities than ours. A possible explanation could be that these authors surveyed a higher redshift range (up to $z \sim 1.9$), where star forming galaxies properties could be significantly different than at $z \sim 0.84$.

The LF corrected for extinction and field to field variance yielded: $\alpha = -1.34 \pm 0.18$, $\phi^* = 10^{-2.76 \pm 0.32}$ Mpc⁻³ and $L^* = 10^{42.97 \pm 0.27}$ erg s⁻¹. The LF extends now to similar luminosities than Hopkins et al. (2000) LF, although, as in the original work no extinction correction was applied, we applied a mean correction $A(\text{H}\alpha) = 1$. However, this mean correction could lead to subestimate L^* , as the highest attenuated sources wouldn't move to their actual high luminosities. On the other hand, we found a mean attenuation for our sample $A(\text{H}\alpha) = 1.45$ whereas we have applied the typical mean correction for the Hopkins et al. (2000) LF.

Analyzing each field independently and compared to the mean density of galaxies we found that there is an overabundance factor of ~ 2.8 , ~ 1.08 and ~ 2.0 for Groth2, Groth3 and GOODS-N fields respectively.

The SFRd derived from the extinction and field to field variance corrected LF is $\dot{\rho}_* = 0.17_{-0.03}^{+0.03}$ M $_{\odot}$ yr⁻¹ Mpc⁻³. The strong increase from $z=0$. to $z \sim 1$ found in other surveys is confirmed. Combining just the H α -based SFR densities obtained by our group from $z = 0.02$, $z = 0.24$, $z = 0.40$ and $z = 0.84$ H α -selected samples, we obtain an evolution of the cosmic SFR density $\propto (1+z)^{\beta}$ where $\beta = 3.8 \pm 0.5$. This β value is similar to the one estimated by Tresse et al. (2002) and by Pérez-González et al. (2005) for thermal IR-selected samples.

The H α approach is complementary to FIR and UV surveys as it reach fainter SFRs than FIR surveys and is less affected by extinction than UV surveys. The fraction of objects detected in FIR not detected by H α is around $\sim 15\%$ unless very high extinguished objects are present, as in the case of GOODS-N.

We thank Nicolas Cardiel and Armando Gil de Paz for advice and useful comments. V. Villar acknowledges the receipt of a *Formación de Personal Investigador* fellowship from the Spanish Ministerio de Educación y Ciencia. This work was supported in part by the Spanish *Plan Nacional de Astronomía y Astrofísica* under grant AYA2003-01676 and AYA2006-02358. This work was supported in part by a generous grant of the *New del Amo Foundation Program*.

Facilities: CAO:3.5m Keck:II

REFERENCES

- Adelman-McCarthy, J. K. et al. 2006, ApJS, 162, 38
 Alexander, D. M. et al. 2003, AJ, 126, 539
 Alonso-Herrero, A. et al. 2006, ApJ, 640, 167
 Arnouts, S. et al. 2005, ApJ, 619, L43
 Baugh, C. M. 2006, Reports of Progress in Physics, 69, 3101
 Bell, E. F. 2003, ApJ, 586, 794
 Bertin, E., & Arnouts, S. 1996, A&AS, 117, 393
 Brinchmann, J., Charlot, S., White, S. D. M., Tremonti, C., Kauffmann, G., Heckman, T., & Brinkmann, J. 2004, MNRAS, 351, 1151
 Buat, V. et al. 2005, ApJ, 619, L51
 Calzetti, D., Armus, L., Bohlin, R. C., Kinney, A. L., Koornneef, J., & Storchi-Bergmann, T. 2000, ApJ, 533, 682
 Calzetti, D. et al. 2005, ApJ, 633, 871
 Capak, P. et al. 2004, AJ, 127, 180
 Charlot, S., & Longhetti, M. 2001, MNRAS, 323, 887
 Chary, R., & Elbaz, D. 2001, ApJ, 556, 562
 Coil, A. L., Newman, J. A., Kaiser, N., Davis, M., Ma, C.-P., Kocevski, D. D., & Koo, D. C. 2004, ApJ, 617, 765
 Cowie, L. L., Barger, A. J., Hu, E. M., Capak, P., & Songaila, A. 2004, AJ, 127, 3137
 Daddi, E., Cimatti, A., Renzini, A., Fontana, A., Mignoli, M., Pozzetti, L., Tozzi, P., & Zamorano, G. 2004, ApJ, 617, 746
 Davis, M. et al. 2007, ApJ, 660, L1
 Doherty, M., Bunker, A., Sharp, R., Dalton, G., Parry, I., & Lewis, I. 2006, MNRAS, 370, 331
 Eisenhardt, P. R. et al. 2004, ApJS, 154, 48
 Erb, D. K., Steidel, C. C., Shapley, A. E., Pettini, M., Reddy, N. A., & Adelberger, K. L. 2006, ApJ, 647, 128
 Faber, S. M. et al. 2003, in Presented at the Society of Photo-Optical Instrumentation Engineers (SPIE) Conference, Vol. 4841, Instrument Design and Performance for Optical/Infrared Ground-based Telescopes. Edited by Iye, Masanori; Moorwood, Alan F. M. Proceedings of the SPIE, Volume 4841, pp. 1657-1669 (2003), ed. M. Iye & A. F. M. Moorwood, 1657-1669
 Ferguson, H. C., Dickinson, M., & Williams, R. 2000, ARA&A, 38, 667
 Gallego, J., Zamorano, J., Aragon-Salamanca, A., & Rego, M. 1995, ApJ, 455, L1+
- Gallego, J., Zamorano, J., Rego, M., & Vitores, A. G. 1997, ApJ, 475, 502
 Gil de Paz, A. et al. 2006, ArXiv Astrophysics e-prints
 Glazebrook, K., Blake, C., Economou, F., Lilly, S., & Colless, M. 1999, MNRAS, 306, 843
 Glazebrook, K., Tober, J., Thomson, S., Bland-Hawthorn, J., & Abraham, R. 2004, AJ, 128, 2652
 Hanish, D. J. et al. 2006, ApJ, 649, 150
 Hopkins, A. M. 2004, ApJ, 615, 209
 Hopkins, A. M., & Beacom, J. F. 2006, ApJ, 651, 142
 Hopkins, A. M., Connolly, A. J., & Szalay, A. S. 2000, AJ, 120, 2843
 Jones, D. H., & Bland-Hawthorn, J. 2001, ApJ, 550, 593
 Kennicutt, Jr., R. C. 1998, ARA&A, 36, 189
 Kong, X., Charlot, S., Brinchmann, J., & Fall, S. M. 2004, MNRAS, 349, 769
 Ly, C. et al. 2007, ApJ, 657, 738
 Meurer, G. R., Heckman, T. M., Leitherer, C., Kinney, A., Robert, C., & Garnett, D. R. 1995, AJ, 110, 2665
 Moorwood, A. F. M., van der Werf, P. P., Cuby, J. G., & Oliva, E. 2000, A&A, 362, 9
 Moustakas, J., Kennicutt, Jr., R. C., & Tremonti, C. A. 2006, ApJ, 642, 775
 Nakamura, O., Fukugita, M., Brinkmann, J., & Schneider, D. P. 2004, AJ, 127, 2511
 Pascual, S. 2005, PASP, 117, 120
 Pascual, S., Gallego, J., Aragon-Salamanca, A., & Zamorano, J. 2001, A&A, 379, 798
 Pascual, S., Gallego, J., & Zamorano, J. 2007, PASP, 119, 30
 Peng, C. Y., Ho, L. C., Impey, C. D., & Rix, H.-W. 2002, AJ, 124, 266
 Pérez-González, P. G., Gallego, J., Zamorano, J., & Gil de Paz, A. 2001, A&A, 365, 370
 Pérez-González, P. G. et al. 2006, ApJ, 648, 987
 —. 2005, ApJ, 630, 82
 Perez-Gonzalez, P. G. et al. 2007, ArXiv e-prints, 709
 Pérez-González, P. G., Zamorano, J., Gallego, J., Aragon-Salamanca, A., & Gil de Paz, A. 2003, ApJ, 591, 827

- Pettini, M., Shapley, A. E., Steidel, C. C., Cuby, J.-G., Dickinson, M., Moorwood, A. F. M., Adelberger, K. L., & Giavalisco, M. 2001, *ApJ*, 554, 981
- Reddy, N. A., Steidel, C. C., Erb, D. K., Shapley, A. E., & Pettini, M. 2006, *ApJ*, 653, 1004
- Reddy, N. A., Steidel, C. C., Pettini, M., Adelberger, K. L., Shapley, A. E., Erb, D. K., & Dickinson, M. 2007, *ArXiv e-prints*, 706
- Rowan-Robinson, M. et al. 2005, *AJ*, 129, 1183
- Schechter, P. 1976, *ApJ*, 203, 297
- Schiminovich, D. et al. 2005, *ApJ*, 619, L47
- Schmidt, M. 1968, *ApJ*, 151, 393
- Shioya, Y. et al. 2007, *ArXiv e-prints*, 709
- Sullivan, M., Treyer, M. A., Ellis, R. S., Bridges, T. J., Milliard, B., & Donas, J. 2000, *MNRAS*, 312, 442
- Takahashi, M. I. et al. 2007, *ApJS*, 172, 456
- Tresse, L. et al. 2007, *A&A*, 472, 403
- Tresse, L., & Maddox, S. J. 1998, *ApJ*, 495, 691
- Tresse, L., Maddox, S. J., Le Fèvre, O., & Cuby, J.-G. 2002, *MNRAS*, 337, 369
- Vitores, A. G., Zamorano, J., Rego, M., Gallego, J., & Alonso, O. 1996, *A&AS*, 120, 385
- Willis, J. P., & Courbin, F. 2005, *MNRAS*, 357, 1348
- Wirth, G. D. et al. 2004, *AJ*, 127, 3121
- Yan, L., McCarthy, P. J., Freudling, W., Teplitz, H. I., Malumuth, E. M., Weymann, R. J., & Malkan, M. A. 1999, *ApJ*, 519, L47
- Yan, R., Newman, J. A., Faber, S. M., Konidaris, N., Koo, D., & Davis, M. 2006, *ApJ*, 648, 281
- Zamorano, J., Gallego, J., Rego, M., Vitores, A. G., & Alonso, O. 1996, *ApJS*, 105, 343
- Zamorano, J., Rego, M., Gallego, J. G., Vitores, A. G., Gonzalez-Riestra, R., & Rodriguez-Caderot, G. 1994, *ApJS*, 95, 387

TABLE 3
OBSERVED SAMPLE

ID (1)	α (J2000) (2)	δ (J2000) (3)	J (4)	$f_{H\alpha}$ (5)	EW(H α) (6)	A(H α) (7)	SFR _{obs} (8)	SFR _{cor} (9)
f2_481	214.39872	52.36067	20.22±0.08	23.6±4.7	67	0.45	4.6	6.9
f2_566	214.49003	52.36594	21.62±0.12	15.4±3.9	209	1.81	3.2	16.9
f2_592	214.28326	52.36750	21.88±0.16	14.1±4.4	241	1.60	3.0	13.0
f2_688	214.26028	52.37098	21.76±0.14	14.1±4.4	121	3.04	2.9	48.4
f2_959	214.44781	52.37737	19.15±0.03	6.8±3.4	17	1.97	1.2	7.4
f2_997	214.43842	52.38060	21.20±0.09	14.2±4.0	132	1.04	2.8	7.3
f2_1238	214.40850	52.38895	19.95±0.05	20.9±5.6	34	2.02	3.9	24.9
f2_1461	214.21682	52.39630	18.95±0.02	53.8±7.8	33	2.08	10.0	68.1
f2_1463	214.40130	52.39658	22.26±0.27	11.1±4.1	282	1.06	2.4	6.4
f2_1650	214.49389	52.40403	21.12±0.09	25.6±6.0	111	1.25	5.3	16.6
f2_1694	214.36583	52.40625	21.12±0.12	14.8±3.8	179	1.41	3.0	11.0
f2_1822	214.20626	52.41180	22.48±0.25	9.2±3.7	273	0.07	2.0	2.1
f2_2091	214.50282	52.41996	21.82±0.19	30.1±4.3	513	0.08	7.2	7.7
f2_2121	214.51324	52.42082	21.70±0.17	12.8±4.1	231	1.65	2.7	12.2
f2_2219	214.25459	52.42487	21.40±0.11	20.0±4.6	115	0.72	4.1	8.0
f2_2362	214.50548	52.42970	21.57±0.12	16.0±4.2	114	1.12	3.3	9.2
f2_2522	214.46666	52.43515	23.48±0.32	10.9±3.2	611	0.23	2.7	3.3
f2_2539	214.50109	52.43483	20.83±0.08	8.1±4.3	32	3.33	1.5	32.4
f2_2556	214.30817	52.43651	22.47±0.21	17.1±4.3	450	0.07	4.0	4.3
f2_2598	214.49855	52.43669	20.71±0.07	18.7±5.6	59	0.92	3.6	8.3
f2_2668	214.31872	52.43925	20.84±0.13	22.4±5.1	189	1.34	4.6	15.6
f2_2706	214.50345	52.44056	20.67±0.09	40.4±7.0	223	1.04	8.4	22.0
f2_2993	214.23302	52.44979	19.86±0.06	20.6±5.8	35	1.75	3.8	19.3
f2_3093	214.24402	52.45767	22.55±0.29	9.3±3.7	275	0.45	2.0	3.0
f2_3166	214.21455	52.45995	21.72±0.21	16.0±5.2	292	0.84	3.5	7.6
f2_3194	214.24633	52.45995	21.16±0.12	10.0±2.9	74	2.46	2.0	18.9
f2_3345	214.25875	52.46516	20.67±0.07	16.1±4.2	52	2.75	3.1	38.7
f2_3358	214.24843	52.46479	20.64±0.09	22.4±5.4	74	2.31	4.4	36.9
f2_3458	214.20323	52.46636	19.19±0.03	27.5±6.6	24	1.47	5.0	19.5
f2_3460	214.53003	52.46774	19.95±0.05	18.8±5.2	37	1.43	3.5	13.1
f2_3507	214.21475	52.47060	19.48±0.04	20.0±5.1	26	1.98	3.7	22.8
f2_3614	214.41869	52.47512	22.75±0.26	7.7±2.5	342	2.24	1.7	13.7
f2_3726	214.36825	52.47954	22.64±0.33	8.3±3.1	340	0.34	1.9	2.6
f2_3742	214.32370	52.47898	21.12±0.11	10.4±3.4	71	2.54	2.0	20.9
f2_3786	214.42755	52.47950	19.44±0.04	60.5±7.4	65	2.16	11.7	86.1
f2_3992	214.28128	52.48944	20.03±0.05	25.8±6.3	43	1.27	4.9	15.6
f2_4054	214.19562	52.49363	22.31±0.22	8.9±3.2	287	0.04	1.9	2.0
f2_4179	214.45653	52.49805	23.14±0.32	12.0±3.9	549	1.41	2.9	10.6
f2_4323	214.25305	52.50370	21.13±0.13	9.7±3.4	77	2.34	1.9	16.5
f2_4422	214.53702	52.50786	23.18±0.32	20.1±3.4	1077	0.38	5.1	7.2
f2_4692	214.23025	52.51940	21.68±0.14	6.1±2.8	129	1.02	1.2	3.0
f2_4713	214.29729	52.51900	20.15±0.07	25.5±5.2	63	0.85	4.9	10.8
f2_4769	214.28798	52.52265	23.26±0.28	8.9±3.2	505	3.74	2.1	65.8
f2_4937	214.30355	52.52710	19.77±0.05	12.6±4.1	27	2.76	2.3	29.2
f2_4986	214.43021	52.52997	22.48±0.21	11.4±3.5	190	1.16	2.6	7.5
f2_5405	214.53927	52.54503	20.83±0.10	18.1±5.6	69	1.12	3.5	9.9
f2_5408	214.53529	52.54495	20.28±0.06	79.5±6.7	167	1.02	17.5	45.1
f2_5459	214.47510	52.54793	22.12±0.18	7.7±4.7	150	0.75	1.5	3.1
f2_5508	214.28716	52.56664	21.12±0.10	35.9±6.1	154	0.63	7.8	14.0
f2_5584	214.30300	52.56433	21.20±0.10	20.0±5.2	95	1.26	4.0	12.8
f2_5594	214.55351	52.56617	22.04±0.25	31.9±8.8	646	0.44	7.8	11.7
f2_5639	214.28714	52.56724	21.16±0.10	11.2±3.8	68	1.04	2.2	5.6
f2_5959	214.29914	52.55195	21.79±0.20	13.8±4.2	136	3.04	2.9	48.2
f2_5993	214.55324	52.54776	19.99±0.06	18.7±9.8	42	2.88	3.5	50.0
f2_7462	214.28432	52.56822	20.50±0.06	27.1±5.0	77	1.26	5.3	17.1
f3_530	214.35434	52.58357	21.47±0.12	27.0±6.2	288	0.68	5.9	11.0
f3_578	214.54496	52.58483	22.35±0.18	12.0±4.3	280	1.31	2.6	8.7
f3_863	214.60952	52.58966	19.46±0.03	17.5±4.8	20	1.34	3.2	10.9
f3_1282	214.66531	52.60264	19.19±0.02	29.3±6.3	25	1.10	5.3	14.8
f3_1316	214.51123	52.60716	21.41±0.09	16.3±3.9	94	4.13	3.3	147.8
f3_1344	214.69324	52.60773	23.53±0.31	11.1±3.3	599	1.25	2.7	8.6
f3_1390	214.37272	52.60940	21.53±0.10	15.2±3.7	99	1.93	3.1	18.1
f3_2440	214.71246	52.64082	20.89±0.07	13.8±4.0	98	1.04	2.6	6.9
f3_2588	214.40606	52.64745	21.81±0.12	10.2±3.6	158	1.06	2.0	5.4
f3_2634	214.65503	52.64757	20.41±0.05	23.0±5.4	98	2.02	4.4	28.2
f3_2635	214.70055	52.64851	22.29±0.14	10.5±3.2	245	1.00	2.2	5.6
f3_2694	214.40516	52.65156	21.87±0.17	9.4±2.8	246	0.58	2.0	3.4
f3_2919	214.66029	52.65804	21.60±0.12	7.4±2.7	123	1.14	1.4	4.1
f3_3041	214.75493	52.66071	21.29±0.11	10.9±4.6	103	0.08	2.1	2.2
f3_3112	214.42338	52.66452	21.34±0.12	4.7±2.2	111	0.92	0.9	2.1
f3_3417	214.57087	52.67417	20.32±0.04	16.2±3.7	41	1.86	3.0	16.9
f3_3525	214.41201	52.67866	21.26±0.10	8.6±2.9	136	1.06	1.7	4.5

NOTE. — (1) Identification (2) RA (J2000) (3) DEC (J2000) (4) J-magnitude (Vega) (5) Line flux ($10^{-17} \text{ ergs}^{-1} \text{ cm}^{-2}$) (6) Restframe equivalent width (Å) (7) Extinction in magnitudes (8) SFR not corrected for extinction ($M_{\odot} \text{ yr}^{-1}$) (9) SFR corrected for extinction ($M_{\odot} \text{ yr}^{-1}$).

TABLE 3
OBSERVED SAMPLE

ID (1)	α (J2000) (2)	δ (J2000) (3)	J (4)	$f_{H\alpha}$ (5)	EW(H α) (6)	A(H α) (7)	SFR _{obs} (8)	SFR _{cor} (9)
f3_3675	214.42497	52.68249	19.15±0.02	28.2±6.7	22	1.29	5.1	16.7
f3_3694	214.40237	52.68428	20.77±0.06	20.6±4.4	69	0.66	4.0	7.3
f3_3972	214.54982	52.69515	21.85±0.15	11.8±3.6	186	0.08	2.4	2.6
f3_4116	214.42933	52.70046	22.28±0.18	8.3±2.8	184	1.54	1.7	6.9
f3_4119	214.75000	52.69880	20.75±0.07	12.6±4.3	79	2.20	2.4	18.1
f3_4133	214.56011	52.70091	22.28±0.17	9.9±3.1	248	0.08	2.1	2.3
f3_4222	214.48923	52.70217	19.91±0.04	22.2±5.6	36	0.52	4.2	6.7
f3_4368	214.42725	52.70791	20.10±0.04	21.4±4.2	46	3.75	4.0	128.2
f3_4659	214.34934	52.71719	20.37±0.06	6.5±6.3	15	4.04	1.1	47.0
f3_4741	214.41970	52.72037	22.27±0.15	20.5±4.2	468	0.08	4.8	5.2
f3_4858	214.37258	52.72191	19.58±0.03	24.2±5.1	30	4.17	4.5	207.6
f3_4891	214.40727	52.72368	19.53±0.02	25.2±5.1	50	1.25	4.6	14.6
f3_4901	214.54208	52.72290	20.72±0.08	6.9±3.0	27	1.96	1.3	7.7
f3_4916	214.63473	52.72382	20.13±0.04	13.1±3.9	27	2.38	2.4	21.5
f3_4927	214.36864	52.72580	21.69±0.12	9.1±3.3	163	0.07	1.8	1.9
f3_4955	214.40295	52.72560	19.63±0.03	20.5±5.2	25	3.58	3.8	101.4
f3_5080	214.60435	52.73046	20.65±0.08	8.6±3.0	79	0.04	1.6	1.7
f3_5362	214.71217	52.74022	21.54±0.16	11.6±4.0	185	1.31	2.4	7.9
f3_5603	214.56435	52.74962	22.61±0.28	6.7±2.5	319	0.95	1.5	3.6
f3_5746	214.75617	52.75273	19.48±0.03	30.6±6.4	30	1.65	5.7	25.9
f3_5781	214.64338	52.75524	21.76±0.12	14.7±4.0	117	1.34	3.1	10.5
f3_5785	214.50875	52.75358	18.97±0.02	7.3±3.2	17	2.33	1.3	11.0
f3_5808	214.48128	52.75600	21.25±0.09	11.7±2.9	159	0.84	2.3	5.0
f3_5857	214.67298	52.75791	21.91±0.13	6.0±2.4	127	1.00	1.2	2.9
f3_5893	214.75849	52.75765	20.74±0.08	6.1±2.7	50	1.14	1.2	3.3
f3_6178	214.38307	52.77068	22.23±0.14	12.1±3.4	288	0.64	2.6	4.7
f3_6456	214.36018	52.82435	22.15±0.15	10.2±3.7	244	0.38	2.2	3.1
f3_6483	214.39506	52.82217	21.80±0.19	4.1±2.2	146	1.41	0.8	3.0
f3_6553	214.46315	52.82027	22.48±0.25	8.7±3.2	285	1.25	1.9	6.0
f3_7108	214.44095	52.80083	21.42±0.13	6.4±2.5	127	0.04	1.2	1.3
f3_7402	214.51934	52.79224	20.14±0.06	4.8±2.2	89	2.06	0.9	6.1
f3_7493	214.47743	52.79039	20.76±0.06	7.4±4.1	46	0.30	1.4	1.8
f3_7702	214.39626	52.78315	19.75±0.04	33.5±6.4	83	1.65	6.3	29.0
g1_375	189.12078	62.08836	21.86±0.30	6.8±3.5	67	1.12	1.3	3.7
g1_456	189.24120	62.09161	22.12±0.29	5.2±2.4	196	1.19	1.1	3.2
g1_465	189.19594	62.09143	20.99±0.12	15.5±4.1	130	1.95	3.0	18.1
g1_496	188.92963	62.09167	19.12±0.05	38.9±9.1	29	2.05	7.2	47.6
g1_516	189.42234	62.09258	20.77±0.12	12.8±4.7	54	1.33	2.4	8.3
g1_713	189.22507	62.10214	20.36±0.12	12.4±3.2	47	2.65	2.3	26.9
g1_908	189.21466	62.11220	19.97±0.08	35.5±5.1	115	2.31	6.8	57.2
g1_1034	189.30751	62.11791	20.88±0.12	15.0±3.5	66	0.58	2.9	5.0
g1_1082	189.14916	62.12032	21.44±0.26	6.8±2.4	124	1.37	1.3	4.7
g1_1159	189.15771	62.12317	20.66±0.12	14.6±3.1	64	1.27	2.8	9.1
g1_1516	189.00670	62.13943	20.59±0.13	14.1±3.9	50	2.01	2.7	17.0
g1_1665	189.12674	62.14533	20.87±0.13	21.4±3.9	86	1.58	4.2	18.2
g1_1735	189.12719	62.14752	20.34±0.11	27.2±4.8	79	3.31	5.4	113.1
g1_1995	189.06608	62.15986	20.93±0.13	23.8±4.6	178	0.79	4.8	9.9
g1_2073	189.39735	62.16152	20.71±0.12	13.4±4.3	66	3.53	2.6	67.0
g1_2141	189.16036	62.16473	18.85±0.04	39.5±6.6	22	1.14	7.2	20.5
g1_2198	189.11342	62.16728	20.39±0.12	18.2±3.9	105	0.48	3.5	5.4
g1_2205	189.35772	62.16781	20.94±0.15	17.2±5.0	171	1.88	3.4	19.5
g1_2339	189.23896	62.17391	20.90±0.16	5.9±2.1	78	1.43	1.1	4.1
g1_2387	188.95030	62.17764	22.01±0.21	12.0±3.2	233	0.79	2.5	5.2
g1_2450	188.94491	62.18024	20.56±0.13	12.1±3.6	43	2.75	2.3	28.5
g1_2537	188.93729	62.18332	21.46±0.17	16.2±3.3	134	1.74	3.4	17.0
g1_2669	189.00505	62.19133	21.77±0.20	10.1±2.8	170	2.36	2.0	17.7
g1_2815	189.15753	62.19707	20.64±0.12	12.8±4.0	85	2.29	2.4	20.0
g1_2827	189.15960	62.19750	20.44±0.11	21.0±4.6	54	3.05	4.0	66.4
g1_2882	189.01208	62.20036	20.63±0.11	17.9±4.0	58	0.87	3.4	7.7
g1_3000	189.42950	62.20486	20.38±0.10	15.7±8.3	66	1.46	2.9	11.2
g1_3068	188.97302	62.20893	20.06±0.09	21.7±4.6	44	0.98	4.1	10.1
g1_3178	189.16642	62.21390	19.55±0.06	17.8±3.5	30	2.41	3.3	30.3
g1_3205	189.28483	62.21460	20.72±0.14	18.0±4.6	59	1.56	3.5	14.6
g1_3339	189.13999	62.22222	19.91±0.07	19.3±4.0	32	2.25	3.6	28.5
g1_3400	189.30463	62.22606	20.96±0.18	20.0±3.8	181	0.79	4.0	8.3
g1_3531	188.95300	62.23167	20.57±0.12	23.4±3.7	164	0.34	4.7	6.4
g1_3581	189.39394	62.23232	19.00±0.05	33.9±10.0	26	1.88	6.2	35.2
g1_3630	189.40551	62.23646	20.31±0.12	9.8 ± 6.3	27	1.06	1.8	4.8
g1_3655	189.27626	62.25499	20.23±0.15	34.2±4.7	180	0.71	6.9	13.2
g1_3693	189.27757	62.25355	21.69±0.30	7.8±3.6	70	1.00	1.5	3.8
g1_3694	189.28492	62.25408	20.29±0.09	50.3±4.9	222	0.98	10.5	25.8

NOTE. — (1) Identification (2) RA (J2000) (3) DEC (J2000) (4) J-magnitude (Vega) (5) Line flux ($10^{-17} \text{ ergs}^{-1} \text{ cm}^{-2}$) (6) Restframe equivalent width (Å) (7) Extinction in magnitudes (8) SFR not corrected for extinction ($M_{\odot} \text{ yr}^{-1}$) (9) SFR corrected for extinction ($M_{\odot} \text{ yr}^{-1}$).

TABLE 3
OBSERVED SAMPLE

ID (1)	α (J2000) (2)	δ (J2000) (3)	J (4)	$f_{H\alpha}$ (5)	EW(H α) (6)	A(H α) (7)	SFR _{obs} (8)	SFR _{cor} (9)
g1_3756	189.36488	62.24973	21.58±0.22	14.7±5.2	261	1.63	3.1	14.1
g1_3779	189.37307	62.24834	21.18±0.16	16.1±6.1	94	0.31	3.2	4.3
g1_4171	189.02571	62.32623	22.01±0.22	3.5±2.5	40	1.28	0.7	2.2
g1_4268	189.27285	62.33080	20.67±0.22	36.1±5.9	278	2.19	7.8	59.0
g1_4284	189.27174	62.33083	20.41±0.19	9.8±3.7	80	0.08	1.9	2.0
g1_4398	189.33542	62.32533	21.85±0.24	11.8±5.0	219	2.23	2.5	19.1
g1_4423	189.39726	62.32167	19.42±0.06	36.7±7.8	42	2.21	6.9	52.8
g1_4558	189.35632	62.31392	19.22±0.05	51.9±8.4	51	2.22	9.9	76.7
g1_4806	189.39811	62.30147	18.99±0.05	32.3±10.6	23	0.94	5.9	14.0
g1_4832	189.32014	62.30673	20.18±0.12	32.9±5.1	179	2.26	6.6	53.3
g1_4908	189.42394	62.29461	21.93±0.21	26.4±6.7	272	2.63	6.3	70.8
g1_5183	189.34373	62.28091	20.86±0.15	16.6±4.7	177	1.04	3.3	8.7
g1_5226	189.17678	62.27920	21.12±0.19	9.7±2.8	64	1.95	1.9	11.2
g1_5276	189.33590	62.27489	20.48±0.13	27.6±7.5	77	2.05	5.4	35.9

NOTE. — (1) Identification (2) RA (J2000) (3) DEC (J2000) (4) J-magnitude (Vega) (5) Line flux ($10^{-17} \text{ ergs}^{-1} \text{ cm}^{-2}$) (6) Restframe equivalent width (Å) (7) Extinction in magnitudes (8) SFR not corrected for extinction ($M_{\odot} \text{ yr}^{-1}$) (9) SFR corrected for extinction ($M_{\odot} \text{ yr}^{-1}$).